Fast Electron Transport in Improved-Confinement RFP Plasmas

by

Daniel J. Clayton

A dissertation submitted in partial fulfillment of the

requirements for the degree of

Doctor of Philosophy

(Physics)

at the

University of Wisconsin – Madison

2010

Fast Electron Transport in Improved-Confinement RFP Plasmas

Daniel J. Clayton

Under the supervision of Professor Cary Forest

At the University of Wisconsin — Madison

Hard-x-ray bremsstrahlung, with photon energies reaching 150 keV, is detected in reversed-field pinch (RFP) plasma discharges with reduced tearing mode amplitudes, indicative of improved confinement of fast electrons compared to the standard case. Current-driven tearing modes in standard RFP plasmas create stochastic magnetic fields; fast electrons, generated by a strong electric field in the plasma core, are nearly collisionless and stream along these stochastic fields, diffusing radially out of the plasma core at a rate proportional to their velocity. In these discharges, emitted x-rays do not exceed energies of about 10 keV. By comparison, when tearing mode amplitudes are sufficiently reduced, magnetic flux surfaces are restored and fast electrons become well-confined, diffusing radially at a rate independent of their velocity. Experiments were performed on the Madison Symmetric Torus RFP using an x-ray spectroscopy diagnostic. Twelve CdZnTe photodiode detectors measure 10-150 keV hard-x-ray bremsstrahlung from fast electrons, and a silicon detector measures 2-10 keV soft-x-ray bremsstrahlung from thermal and fast electrons. The detectors are placed primarily along a radial array of beryllium x-ray windows. They are run in pulse mode, and the signals are digitized to enable the separation of pulses from noise

and the resolution of pulse pileup. Pulse heights are proportional to x-ray energy and are calibrated with a known source, and pulses are binned by time, energy, and radius to obtain spectra. Hard x rays are measured from the core of discharges with pulsed parallel current drive, which modifies the current profile to reduce tearing mode amplitudes and thus magnetic stochasticity. In these discharges, the Fokker-Planck code CQL3D can be used to infer the effective ion charge Z_{eff} and the particle diffusion coefficient D_r. Hard x rays are also detected when a large magnetic island forms in the plasma core, usually the result of quasi-single helicity, where one tearing mode grows large while the rest are suppressed. Stochasticity is reduced within the magnetic island and fast electrons are well-confined in this region.

Cary Forest (Adviser)

Acknowledgments

I would like to thank the entire MST team for their guidance and support throughout my years as a graduate student. In particular:

Thank you to my first advisor, Stewart Prager, for piquing my interest in plasma physics with his introductory course my first year in Madison.

Thank you to my second advisor, Cary Forest, for teaching an old graduate student new tricks.

Thank you to Rob O'Connell, my first mentor, for teaching me many of the skills I will use as a scientist.

Thank you to Abdulgader Almagri, my second mentor, for lending me his hardware expertise and for carefully reading everything I wrote.

Thank you to the lower hybrid group: John Goetz, John Kulpin, Mike Kaufman, and especially Dave Burke, for all of their time and energy spent improving the x-ray diagnostic.

Thank you to Caroline Ubing for the endless SolidWorks drawings.

Thank you to Brett Chapman for helping me sift through the seemingly senseless QSH data and making sense of it all.

Thank you to Paolo Franz, Paolo Piovesan, and Federica Bonomo for working with me to correlate the spectroscopic and tomographic data, and to Marco Gobbin for the insightful ORBIT results.

Thank you to all the diagnosticians, particularly the graduate students who spent so many run days collecting data for me: Josh Reusch and Hillary Stephens for Thomson scattering, Travis Yates for FIR, Rich Magee for CHERS, and Kyle Caspary for MSE.

Thank you to Paul Wilhite, Andrey Levochkin, and especially Alex Squitieri for all of their computer hacking and digitizer help.

Thank you to Peter Weix and John Laufenberg for teaching me the inner workings of MST, and to Bill Zimmerman for teaching me the difference between a wrench and a screwdriver.

Thank you to Dale Schutte, Jane Schwantz, and Russ Rylander for all of their assistance, particularly with all of my complicated hardware purchases and travel arrangements.

Thank you to my office mates and three of my best friends: Matt Miller, Josh Reusch, and Tim Tharp.

Thank you to my family: to my parents for encouraging me to pursue a career in science, to my wife Jessica for all of her love and support, as well as her incredible patience waiting for me to graduate three years later than her, and to my beautiful baby daughter Samantha, for motivating me to finish up and get a real job.

Contents

Chapter 1

Introduction

Plasma, defined as a gas of partially or fully ionized atoms, is often studied in the laboratory for its applicability to fusion energy. To achieve fusion in a reactor, the fusible material must be extremely hot; at these high temperatures atoms become fully ionized and form a plasma. This hot plasma must somehow be confined within the reactor long enough for fusion to occur. One possible path to a fusion reactor is through magnetic confinement of the plasma. To first order, charged particles move along magnetic field lines, thus magnets can be used to confine a hot fusion plasma. The most common type of magnetic confinement device is a torus, with toroidal and poloidal magnetic fields creating a closed loop of plasma current. For fusion to be successful, the plasma must be hot enough, dense enough, and confined long enough for the ions to fuse. Radial diffusion of high energy particles must be kept to a minimum. Thus it is important to understand the mechanisms by which particles are transported radially in a plasma device.

While particle collisions are an obvious source of radial particle diffusion, in most toroidal experiments they are not the dominant source. Instead, the radial transport of particles is dominated by fluctuations in the plasma, both electrostatic and magnetic.

One way to study particle transport caused by these fluctuations is through the use of fast electrons. High energy electrons are nearly collisionless, thus their diffusion is due almost entirely to electromagnetic fluctuations. The diffusion of fast electrons can be obseverd experimentally by the x-ray bremsstrahlung that they emit.

On the Madison Symmetric Torus (MST) reversed-field pinch, a toroidal plasma device, fast electron transport is monitored by a set of CdZnTe hard-x-ray detectors. No hard x rays are detected during standard discharges, indicating a diffusion rate so large that fast electrons are lost from the plasma before reaching energies sufficient to emit hard x rays. However, for two special cases in which magnetic fluctuations are reduced in the plasma, x-rays with energies up to 150 keV are detected, indicating a significant reduction in fast electron diffusion and an improvement in particle confinement.

1.1 The Reversed-Field Pinch

The reversed-field pinch (RFP) is a toroidal plasma configuration studied for its potential use in a fusion reactor. It is characterized by poloidal and toroidal magnetic fields of similar magnitude and by reversal of the toroidal field near the edge relative to its direction in the core, as shown in Fig. 1.1(a) [1]. A major advantage over the more common tokamak configuration is its small field size, which is generated primarily by the plasma current rather than bulky, expensive, external field coils. The parallel current density profile is sustained by a $\langle \tilde{v} \times \tilde{b} \rangle$ mean-field electromotive force (emf) [2], such that

$$E_\parallel + \left\langle \tilde{v} \times \tilde{b} \right\rangle_\parallel = \eta J_\parallel. \tag{1.1}$$

In a standard RFP plasma, these fluctuations are created by $m = 1$ tearing modes driven by the current gradient. These fluctuations form islands on numerous rational surfaces in the plasma core, the locations of which are shown on a plot of the q profile in Fig. 1.1(b). These islands generally overlap, destroying the flux surfaces and producing a stochastic field with rapid Rechester-Rosenbluth-like particle transport [3, 4]. This is the major disadvantage of the RFP configuration.

Most research currently performed on RFP experiments involves two possible routes to reducing these magnetic fluctuations, and thus restoring flux surfaces and reducing energy and particle transport. The first is to modify the current profile such that $E_\parallel = \eta J_\parallel$, thus eliminating the need for the $\langle \tilde{v} \times \tilde{b} \rangle$ emf. This has been accomplished successfully, at least transiently, through inductive current drive known as PPCD, or pulsed parallel current drive [5]. With PPCD, tearing mode amplitudes have been largely suppressed and energy confinement times improve by an order of magnitude. This is discussed in more detail in Chapter 4. The second route to reducing tearing mode amplitudes is through single helicity. MHD simulations show that in some situations, the $\langle \tilde{v} \times \tilde{b} \rangle$ emf can be sustained by a single tearing mode, while the other modes disappear [6, 7]. Experimentally, quasi-single helicity (QSH) is sometimes observed, where one mode dominates the tearing mode spectrum, and the others are suppressed, though they do not completely disappear [8]. In this case, a large helical island forms around the resonant surface of the dominant mode, inside which stochasticity may be reduced. This is described in detail in Chapter 5. In both

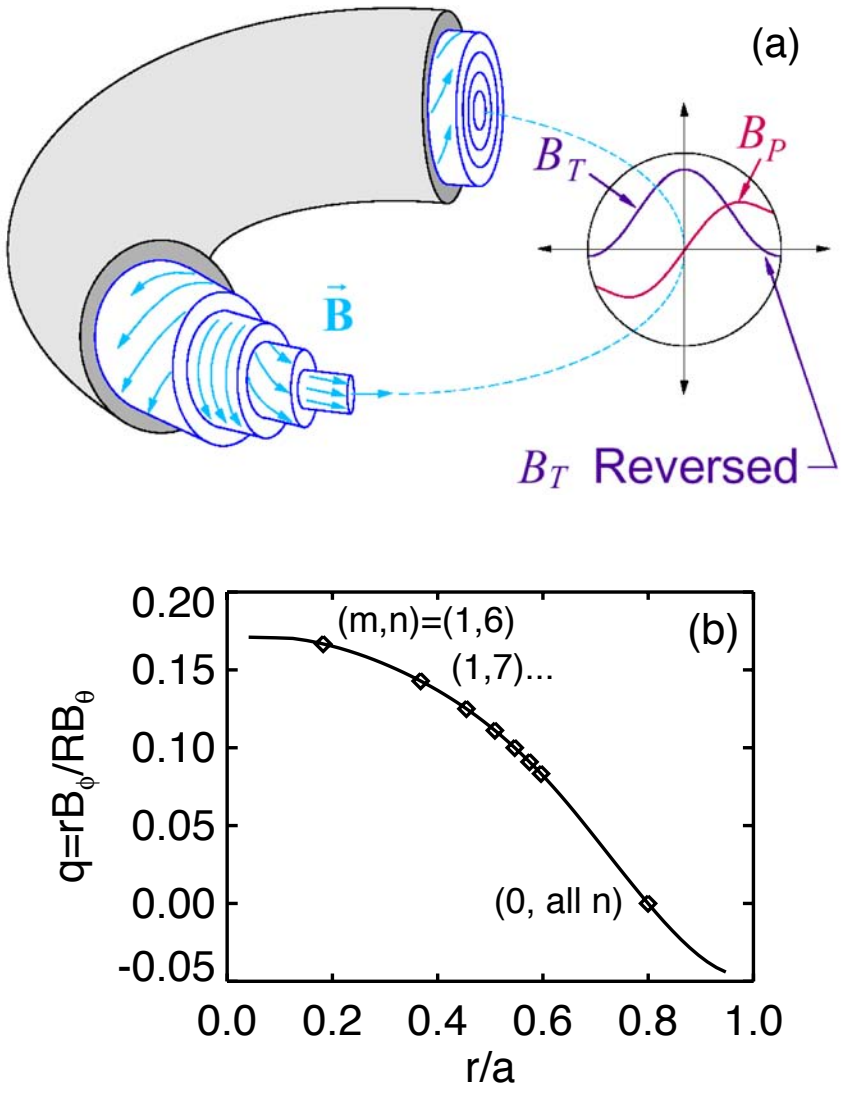

Figure 1.1: (a) A diagram of the magnetic fields in a standard RFP discharge. (b) A safety factor (q) profile, with points indicating the rational surfaces where major tearing modes are resonant. All $m = 0$ modes are resonant at the reversal surface, where $q = 0$.

cases, the change in confinement can be monitored with the help of fast electrons.

1.2 Fast Electron Generation in an RFP

When an electric field is applied to a plasma, the usual Maxwellian electron distribution function becomes distorted. The electric field accelerates fast electrons, the fastest of which can become runaway electrons. An electron runs away when its acceleration due to the electric field exceeds its deceleration from dynamical friction due to Coulomb collisions [9]. The motion of an electron due to these two forces can be written out in the form of Newton's second law as

$$m_e \frac{d\vec{v}}{dt} = q_e \vec{E} - \nu_S^e m_e \vec{v}, \tag{1.2}$$

where ν_S^e is the electron collisional slowing-down frequency [9]. Note that the highest energy runaway electrons measured in MST reach about 150 keV; the relativistic factor $\gamma = 1.29$ in this case, and will be ignored in the following simple estimations. In the parallel direction, Eq. 1.2 becomes

$$m_e \frac{dv_\parallel}{dt} = eE_\parallel - \nu_S^e m_e v_\parallel. \tag{1.3}$$

For runaway electrons, the slowing down frequency due to drag from both electrons and ions can be written as [9]

$$\nu_S^e = \left(1 + \frac{2}{Z_i}\right)\nu(v) = \left(1 + \frac{2}{Z_i}\right)\nu(v_{Te})\frac{v_{Te}^3}{v^3} \qquad v \gg v_{Te}, \tag{1.4}$$

where ν is the Lorentz collision frequency:

$$\nu(v) \equiv \frac{4\pi n_e Z_i e^4 \ln\Lambda}{(4\pi\epsilon_0)^2 m_e^2 v^3}. \tag{1.5}$$

Electrons run away when their speed is large enough that the collisional drag becomes less than the acceleration due to the electric field. This happens when [9]

$$\frac{m_e v^2}{2T_e} > (2 + Z_i)\frac{E_D}{|\vec{E}|}, \tag{1.6}$$

where the Dreicer field E_D is defined as

$$E_D \equiv \frac{2\pi n_e e^3 \ln\Lambda}{(4\pi\epsilon_0)^2 T_e} = \frac{m_e v_{Te}\nu(v_{Te})}{eZ_i}. \tag{1.7}$$

Eq. 1.6 can be used to calculate expected runaway populations in MST. For a standard 400 kA MST discharge, the core electric field is approximately 1.5 V/m, which is sufficiently large to generate runaway electrons. Fig. 1.2(a) shows the relative strengths of the electric and collisional drag forces along the magnetic axis. The point where they cross is the critical energy at which electrons run away. Moving away from the magnetic axis, the critical energy increases as the strength of the electric field decreases, as shown in Fig. 1.2(b). Nearer to the edge of the plasma, the critical energy begins to drop as particle density, and thus collisional drag, decreases. Assuming a Maxwellian electron distribution, Fig. 1.2(c) shows the density of electrons that exceed the critical energy. There are no expected runaways in the edge of the plasma because the temperature and density are much lower than in the core, were many more electrons exceed the critical energy threshold. Fig. 1.2(d)–(f) provide a comparison to an improved-confinement PPCD discharge, where the electric field is reduced to about 0.5 V/m on axis. It is clear that a large number of runaways are

expected in either case; however, far fewer runaways are actually detected, and none are detected in the standard discharge case. This is due to rapid radial transport.

1.3 Using Fast Electrons to Probe Transport

Since fast electrons are nearly collisionless, they make an ideal tool for studying anomalous particle transport. In the absence of collisions, fast electrons are essentially tied to magnetic field lines. If magnetic fluctuations are large enough that flux surfaces are destroyed, fast electrons will diffuse radially at a rate proportional to the diffusion of the field lines [3]. As they follow the field lines, the faster electrons diffuse more quickly, thus the rate of diffusion is also proportional to an electron's parallel velocity. This essentially eliminates fast electrons from the plasma: as electrons begin to run away, they quickly diffuse out of the core of a toroidal plasma with destroyed flux surfaces. This is the case in standard RFP plasmas. Conversely, toroidal discharges that generate fast electrons must have closed flux surfaces in at least some region of the plasma, and in this region magnetic fluctuations no longer dominate electron transport.

1.3.1 X-Ray Bremsstrahlung from Fast Electrons

While fast electrons are not detectable directly, they can be observed via the x rays they emit. X-ray measurements have been used by several plasma experiments, particularly tokamaks, as a means of studying magnetic stochasticity and particle confinement [10–16]. Measured emission may come from fast electron-ion bremmstrahlung, as is the case with most measurements in MST, or from fast electrons striking plasma limiters (thick-target bremsstrahlung), as is the case with the insertable

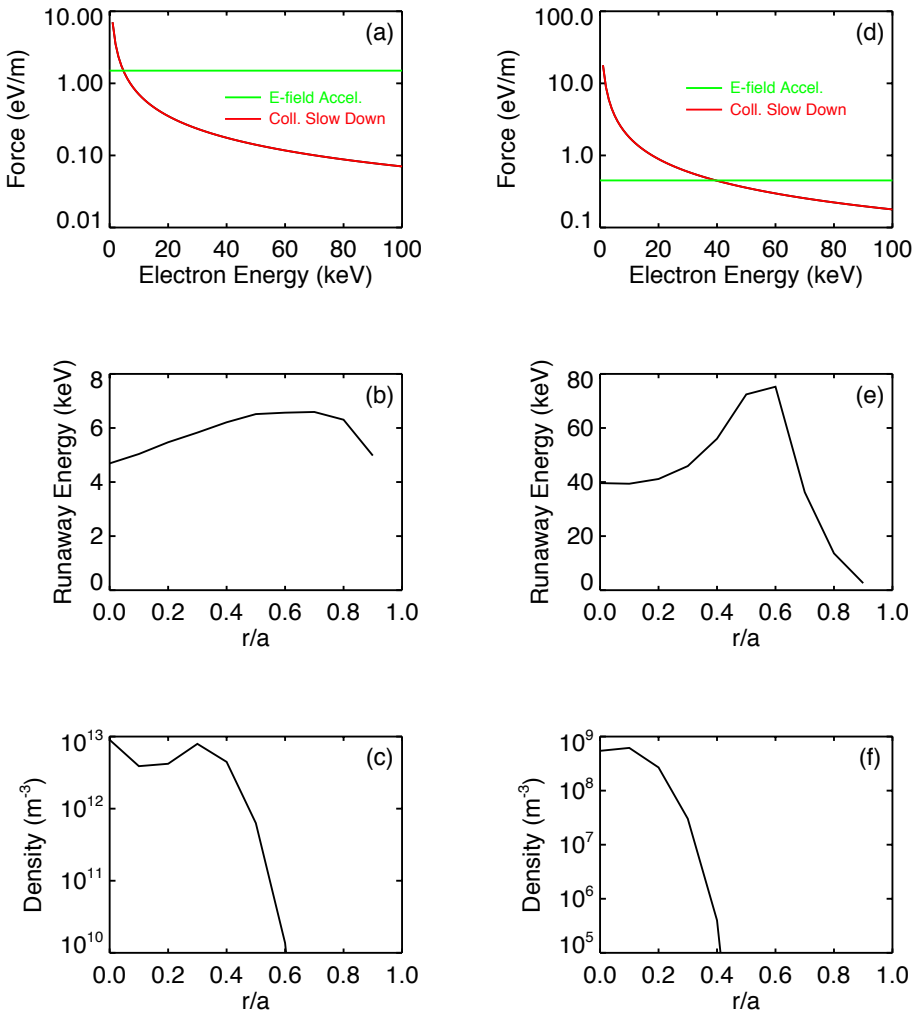

Figure 1.2: (a) A comparison of the parallel electric field and friction forces in the core of a standard 400 kA MST discharge. (b) A radial profile of the critical runaway energy. (c) Density of electrons that exceed the critical energy. (d)–(f) The same for a 400 kA PPCD discharge.

probe discussed in Chapter 5.

Runaway electrons were first observed experimentally in the 1950s in the B-1 stellarator by measuring x-rays from the electrons striking the wall [10]. In the early 1970s, Fokker-Planck modeling was first used to extract a diffusion coefficient from x-ray bremsstrahlung in the ST tokamak, though anomalous transport was not considered [11]. The in the late 1970s, x-ray measurements from the limiter of the ORMAK tokamak revealed diffusion coefficients that were much larger than could be explained [12]. In more recent times, insertable probes were used to measure magnetic field fluctuations in the edge of L-mode ASDEX plasmas, where it was discovered that magnetic turbulence dominated fast electron transport [14]. Diverter measurements from TEXT revealed that magnetic turbulence dominated fast electron diffusion in the edge, though thermal electron diffusion was dominated by electrostatic fluctuations [15]. In TEXTOR, synchrotron radiation measurements from very fast electrons demonstrated that when the magnetic field lines were stochasticized by pellet injection, fast electrons remained confined inside remnant island structures [17]. Otherwise, runaway diffusion rates were extremely small ($D_r < 0.01$ m^2 s^{-1}) [18]. X-ray measurements from the core of JET have shown that electrostatic transport dominates fast electron diffusion in most cases [16]. In summary, x-ray measurements in tokamaks have shown that fast electrons are well confined, except for cases such as the edge of L-mode plasmas, where magnetic perturbations are largest.

Bremsstrahlung is defined as the radiation emitted by an electron accelerated by the electric field of another particle during a Coulomb collision [19]. For a plasma with a Maxwellian electron distribution function, the bremsstrahlung emissivity as a

function of frequency ν is [19]

$$4\pi j(\nu) = n_e^2 Z_{eff} \left(\frac{e^2}{4\pi\epsilon_0}\right)^3 \frac{32\pi^2}{3\sqrt{3}m_e^2 c^3} \left(\frac{2m_e}{\pi T_e}\right)^{1/2} e^{-h\nu/T_e} \bar{g}, \tag{1.8}$$

where $j(\nu)$ is radiated power per unit solid angle, per unit frequency, and per unit volume. The Maxwellian-averaged Gaunt factor $\bar{g} \approx 1$ for x-rays and is very slow-varying. Thus the emissivity primarily depends on the distribution of the electrons (temperature and density for the case of a Maxwellian) and the effective ion charge Z_{eff}. A detailed description of bremsstrahlung, including relativistic and non-Maxwellian electrons, can be found in Ref. [20]. The x-ray bremsstrahlung module of the CQL3D code, which is used to infer Z_{eff} and the electron distribution function from x-ray spectra measured in MST, uses the results from this reference in its calculations.

1.3.2 Finding the Diffusion Coefficient

The mere presence of high energy x-rays is an indication of good flux surfaces and particle transport that is not dominated by magnetic fluctuations. Furthermore, measured x-ray spectra can be used to infer the rate of radial particle diffusion if the electron distribution function is properly modeled. Quantitatively, the time evolution of the distribution function can be described by a kinetic equation [21, 22]:

$$\frac{df}{dt} = \frac{\partial f}{\partial t} + \frac{d\vec{x}}{dt} \cdot \nabla_x f + \frac{d\vec{v}}{dt} \cdot \nabla_v f = \nabla_v \cdot \Gamma_v + R(f) + S \tag{1.9}$$

or

$$\frac{\partial f}{\partial t} + \vec{v} \cdot \nabla_x f + \frac{q}{m}\left(\vec{E} + \frac{\vec{v}}{c} \times \vec{B}\right) \cdot \nabla_v f = \nabla_v \cdot \Gamma_v + R(f) + S. \tag{1.10}$$

The terms on the right-hand side of Eq. 1.10 encompass discrete particle effects on the evolution of the distribution function. Γ_v can be thought of as a current density in velocity space [22], and the $\nabla_v \cdot \Gamma_v$ term represents the effects of particle collisions on the velocity distribution. Effects due to rf wave interactions and synchrotron radiation will be ignored in this thesis. $R(f)$ is a spatial diffusion term; for a toroidal confinement device, this represents a radial diffusion, as particles are expected to quickly equilibrate along a flux surface. S is a particle source/sink term that will also be ignored in this thesis. With the proper collision term, Eq. 1.10 takes the form of a Fokker-Planck equation. This will be discussed further in Chapter 4, which describes the use of the Fokker-Planck code CQL3D to numerically solve for the electron distribution function and the fast electron diffusion coefficient.

1.4 Fast Electron Transport in an RFP

Fast electron transport is monitored in MST with an x-ray spectroscopy diagnostic. In standard MST plasmas, no x-rays with energies greater than 10 keV are detected. This is indicative of the large amount of magnetic stochasticity throughout the plasma volume. Magnetic fluctuations dominate particle transport, and any fast electrons diffuse out of the core of the plasma before they reach high energies. This is in contrast to two special types of plasmas, one with current profiles modified by PPCD and another with large magnetic islands, that both exhibit large fluxes of hard x-rays, with energies up to 150 keV. In these plasmas, magnetic stochasticity is greatly reduced, at least in some region of the plasma, closed flux surfaces are restored, and particle confinement vastly improves.

Previous work on MST, using a single hxr detector with no apertures or filters

(except for the thin aluminum x-ray window) and with a line of sight through the magnetic axis, has shown that fast electron diffusion is greatly reduced and becomes velocity-independent during PPCD [23]. Using the CQL3D code, with a guess for Z_{eff}, D_r was found to be of order 1 m^2/s during PPCD, though the CQL3D model did not properly fit the data at high energies, as shown in Fig. 1.3. This work left several interesting unanswered questions:

- *Why did the x-ray flux not match the CQL3D model at high energies?*
- *How might apertures and filters, which are required to measure larger fluxes without saturating the detector amplifiers, affect the measurements?*
- *What does an array of detectors reveal about the radial profile of hxr flux during PPCD?*
- *With the addition of a soft-x-ray detector to expand the measured spectrum, can CQL3D be used to find Z_{eff}, thus allowing for a more accurate measurement of D_r?*
- And finally, *do other types of RFP plasmas emit hard x rays, an indication of reduced stochasticity and improved confinement? Do these plasmas behave in a fashion similar to PPCD plasmas?*

These questions will all be addressed in the following chapters, and the answers are summarized in the final chapter.

Chapter 2 introduces MST, the reversed-field pinch in which the following experiments were conducted, as well as providing a brief description of various plasma

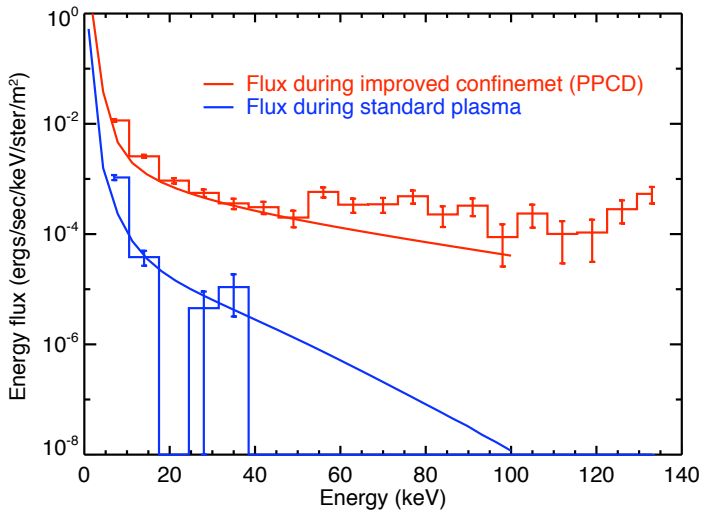

Figure 1.3: Previous work has shown that hxr spectra measured during PPCD (in red) indicate a diffusion coefficient independent of electron velocity, while standard plasmas (in blue) have diffusion coefficients directly proportional to velocity. The points are data, and the solid lines are predicted spectra from CQL3D. Note that at high energies, the measured PPCD flux begins to diverge from the predicted values. Also note that most standard plasmas do not emit any hxrs; those shown in this plot most likely originated in a magnetic island, as discussed in Chapter 5.

diagnostics used in the subsequent analyses. Chapter 3 describes in detail the x-ray spectroscopy diagnostic on MST that is used to monitor fast electrons. Chapter 4 discusses results from plasmas with induced current profile modifications via PPCD, and Chapter 5 discusses results from plasmas with spontaneous formation of magnetic islands. Chapter 6 provides a summary and concluding remarks. Also included is Appendix A, which discusses x-ray radiation doses around MST.

References

[1] H. A. B. Bodin and A. A. Newton, Nucl. Fusion **20**, 1255 (1980).

[2] J. K. Anderson, T. M. Biewer, C. B. Forest, R. O'Connell, S. C. Prager, and J. S. Sarff, Phys. Plasmas **11**, L9 (2004).

[3] A. B. Rechester and M. N. Rosenbluth, Phys. Rev. Lett. **40**, 38 (1978).

[4] T. M. Biewer, C. B. Forest, J. K. Anderson, G. Fiksel, B. Hudson, S. C. Prager, J. S. Sarff, J. C. Wright, D. L. Brower, W. X. Ding, and S. D. Terry, Phys. Rev. Lett. **91**, 045004 (2003).

[5] J. S. Sarff, S. A. Hokin, H. Ji, S. C. Prager, and C. R. Sovinec, Phys. Rev. Lett. **72**, 3670 (1994).

[6] S. Cappello and R. Paccagnella, Phys. Fluids B **4**, 611 (1992).

[7] J. M. Finn, R. Nebel, and C. Bathke, Phys. Fluids B **4**, 1262 (1992).

[8] P. Martin, L. Marrelli, G. Spizzo, P. Franz, P. Piovesan, I. Predebon, T. Bolzonella, S. Cappello, A. Cravotta, D. F. Escande, L. Frassinetti, S. Ortolani, R. Paccagnella, D. Terranova, the RFX team, B. E. Chapman, D. Craig, S. C. Prager, J. S. Sarff, the MST team, P. Brunsell, J.-A. Malmberg, J. Drake, the

EXTRAP T2R team, Y. Yagi, H. Koguchi, Y. Hirano, the TPE-RX team, R. B. White, C. Sovinec, C. Xiao, R. A. Nebel, and D. D. Schnack, Nucl. Fusion **43**, 1855 (2003).

[9] J. D. Callen, Fundamentals of plasma physics, unpublished book available at http://homepages.cae.wisc.edu/∼callen/book.html.

[10] W. Bernstein, F. F. Chen, M. A. Heald, and A. Z. Kranz, Phys. Fluids **1**, 430 (1958).

[11] R. M. Kulsrud, Y.-C. Sun, N. K. Winsor, and H. A. Fallon, Phys. Rev. Lett. **31**, 690 (1973).

[12] S. J. Zweben, D. W. Swain, and H. H. Fleischmann, Nucl. Fusion **18**, 1679 (1978).

[13] H. Knoepfel and D. A. Spong, Nucl. Fusion **19**, 785 (1979).

[14] O. J. Kwon, P. H. Diamond, F. Wagner, G. Fussmann, ASDEX, and N. Teams, Nucl. Fusion **28**, 1931 (1988).

[15] J. R. Myra, P. J. Catto, A. J. Wootton, R. D. Bengtson, and P. W. Wang, Phys. Fluids B **4**, 2092 (1992).

[16] B. Esposito, R. M. Solis, P. van Belle, O. N. Jarvis, F. B. Marcus, G. Sadler, R. Sanchez, B. Fischer, P. Froissard, J. M. Adams, E. Cecil, and N. Watkins, Plasma Phys. Control. Fusion **38**, 2035 (1996).

[17] R. Jaspers, N. J. L. Cardozo, K. H. Finken, B. C. Schokker, G. Mank, G. Fuchs, and F. C. Schüller, Phys. Rev. Lett. **72**, 4093 (1994).

[18] I. Entrop, N. J. L. Cardozo, R. Jaspers, and K. H. Finken, Plasma Phys. Control. Fusion **40**, 1513 (1998).

[19] I. H. Hutchinson, *Principles of Plasma Diagnostics*, Cambridge University Press, second edition (2002).

[20] H. W. Koch and J. W. Motz, Rev. Mod. Phys. **31**, 920 (1969).

[21] R. W. Harvey and M. G. McCoy, in *Proc. of IAEA TCM on Advances in Simulation and Modeling of Thermonuclear Plasmas, Montreal, 1992*, pages 489–526, IAEA, Vienna (1993).

[22] G. D. Kerbel and M. G. McCoy, Phys. Fluids **28**, 3629 (1985).

[23] R. O'Connell, D. J. D. Hartog, C. B. Forest, J. K. Anderson, T. M. Biewer, B. E. Chapman, D. Craig, G. Fiksel, S. C. Prager, J. S. Sarff, and S. D. Terry, Phys. Rev. Lett. **91**, 045002 (2003).

Chapter 2

The Madison Symmetric Torus

The Madison Symmetric Torus (MST) [1] is a reversed-field pinch toroidal plasma confinement device. Located at the University of Wisconsin-Madison, MST is involved in both basic plasma physics and fusion energy research. Distinguishing it from other major RFPs, an iron core transformer and thick conducting shell are used to create the equilibrium fields. The lack of external field coils allows easy access for several plasma diagnostics. MST was originally built to study the effect of large plasma size on RFP confinement [1], though several major modifications and new diagnostics have kept MST in the forefront of RFP research more than twenty years after its first plasma.

This chapter describes the machine itself, as well as several diagnostics utilized in the analyses in subsequent chapters. Sections 2.2 and 2.3 describe diagnostics used for modeling with CQL3D, as discussed in Chapter 4. Section 2.4 describes the soft-x-ray tomography diagnostic, used in Chapter 5 to identify plasmas with a magnetic island. This is a separate diagnostic from the x-ray spectroscopy diagnostic described in detail in the next chapter.

2.1 The Machine

The MST vacuum vessel, or shell, is a 5 cm thick aluminum torus with a major radius of 1.5 m and a minor radius of 0.52 m. The shell consists of two halves bolted together at the midplane, allowing the top half to be lifted for major modifications and upgrades. A 1.3 cm insulated gap, known as the toroidal gap, is left between the two halves on the inboard side where current from the B_T circuit enters and leaves the shell. Also splitting the vessel is the poloidal gap, a 1.3 cm insulated vertical gap that allows poloidal flux from the iron core transformer to enter the machine. In both cases, Viton gaskets are used as both vacuum seals and electrical insulators in these gaps. One hundred ninety-three 3.8 cm diameter holes at the bottom of the shell are enclosed by a pumping manifold that is welded to the vessel. Turbomolecular pumps and cryopumps are used to maintain vacuum. Hundreds of diagnostic ports have been drilled into the vessel, though like the pumping holes, these have been kept small, most less than 5 cm in diameter, to minimize field errors at the plasma boundary.

Besides vacuum containment, the aluminum vessel serves two other important functions. The first is as a close fitting conducting shell to help stabilize resistive wall modes, eliminating the need for a vertical field coil. The second is to act as a single turn toroidal field coil. The toroidal magnetic field is created by sending a poloidal current through the shell, fed by an axisymmetric toroidal flange connected to the toroidal gap. The primary B_T capacitor bank fires through the beginning of the discharge to create the initial toroidal field. A smaller B_T crowbar capacitor bank is sometimes used to sustain field reversal late in the discharge by sending current in the reversed direction. The PPCD system, described in Chapter 4, also feeds into the

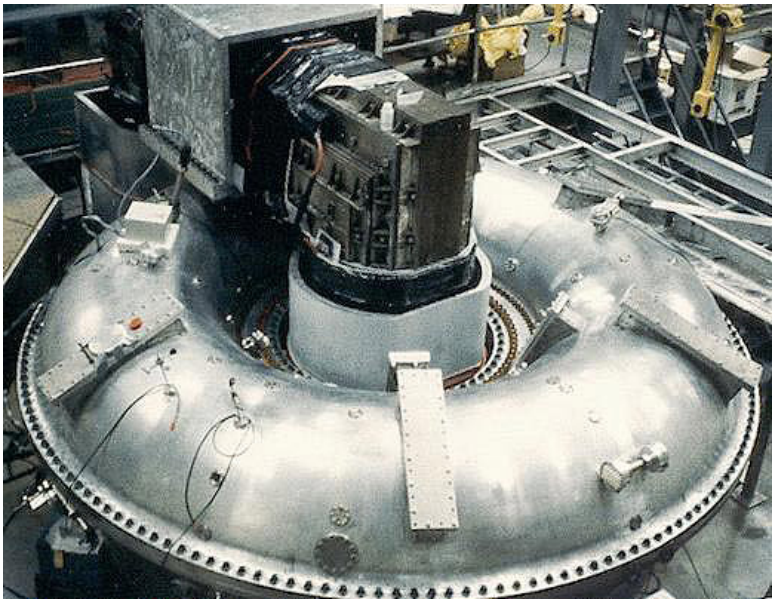

Figure 2.1: A photo of MST before diagnostics were installed. The aluminum shell and iron transformer are clearly visible.

toroidal flange to create poloidal currents in the shell. Currently, a new programmable power supply (PPS) is being tested to replace of all of these systems. This has the advantage of being able to produce arbitrary current waveforms rather than relying on the pulsed discharges of a discrete number of capacitor banks.

The poloidal field is induced by an iron core transformer that surrounds the poloidal gap. Three distinct sets of coils wrap around the iron core. The first is the continuity winding, or C-winding. The function of the C-winding is to carry wall currents across the poloidal gap. Without the C-winding, image currents on the inside surface of the vacuum vessel would flow to the outside of the shell at the poloidal gap, creating an error field. A poloidal flange distributes current from one side of the gap to the four symmetric sections of the C-windings surrounding the core, then returns the current to the other side of the gap. Outside of the C-winding is the poloidal field

winding itself. The PF-winding consists of forty copper bars that sit on a theoretical flux surface outside of the shell. They act like a 40:1 transformer, with the plasma acting as the secondary. A large current is pulsed through the PF-windings, which induces the toroidal plasma current and in turn the poloidal magnetic field. The copper bars pass through the poloidal flange, with the poloidal gap allowing the field to pass into the shell. Finally, inside the C-winding is the bias winding, which reverse biases the iron core to allow a full 2 Wb magnetic flux swing during a discharge.

Power to the PF-winding is provided by four large capacitor banks. Depending on the number of banks and voltages used, the system can create a discharge that lasts between 50 and 80 ms, with a plasma current ranging from 200 to 600 kA. Deuterium gas puffers fuel the plasma, producing electron densities that are typically $0.5–2.0 \times 10^{19}$ m^{-3}, though densities as large as 7×10^{19} m^{-3} have been obtained using deuterium pellet injection. This produces a plasma with electron and ion temperatures in the range of a few hundred electron volts.

2.2 Temperature and Density Measurements

MST has an array of diagnostics to measure the temperature and density of the plasma as a function of radius. They provide a spatially and temporally resolved picture of the bulk, Maxwellian, electron and ion distribution functions which is used with the Fokker-Planck code CQL3D, as described in Chapter 4.

2.2.1 Electron Temperature: Thomson Scattering

Electron temperature is measured with a multipoint Thomson scattering diagnostic [2–5]. Two Nd:YAG lasers each fire one or multiple pulses of 1064 nm infrared

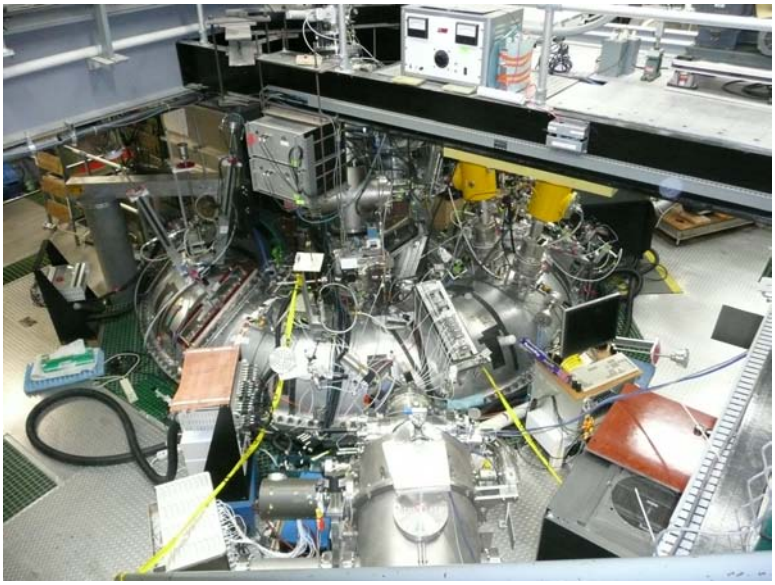

Figure 2.2: A recent photo of MST with all of the diagnostics installed.

light, each pulse with an energy on the order of a joule. A small fraction of the photons from these pulses scatter off electrons in the plasma (Thomson scattering refers to the classical scattering of photons off charged particles), and a set of collection optics measures the scattered light from 21 points along the beam path, covering the entire minor radius. Fiber-optics carry the signal from each radial point to a set of spectrometers. It can be shown that the frequency of a scattered photon is just

$$\omega_s = \omega_i + \boldsymbol{k} \cdot \boldsymbol{v} = \omega_i + (\boldsymbol{k_s} - \boldsymbol{k_i}) \cdot \boldsymbol{v}, \tag{2.1}$$

where $\boldsymbol{k_i}$ and $\boldsymbol{k_s}$ are the wave vectors of the incident and scattered photons and $\boldsymbol{v}$ is the velocity of the electron [6]. This can be thought of as a Doppler shift due to the relative motions between the incident photon and electron and the emitted photon and electron. Since the wave vectors of the incident photons are known, the electron distribution function can thus be found from the distribution of the scattered light.

At this time the diagnostic is not calibrated to provide electron density, but the width of the measured distribution is proportional to electron temperature.

2.2.2 Majority Ion Temperature: Rutherford Scattering

The temperature of the majority ion species in the plasma (deuterium) is measured with a Rutherford scattering diagnostic [7, 8]. A monoenergetic beam of high energy neutral helium atoms is injected into MST [9]. These helium neutrals scatter off the majority ions due to Coulomb collisions with a known cross section. Some of the scattered helium atoms are collected by two neutral particle analyzers, which strip the helium atoms and use 12-channel electrostatic energy analyzers to measure their energy distribution. The width of this Gaussian distribution is proportional to the square root of the deuterium ion temperature [7].

2.2.3 Impurity Ion Temperature: CHERS

The temperature of impurity ions, primarily fully stripped carbon ions (C^{+6}), is measured with a charge exchange recombination spectroscopy (CHERS) diagnostic [8, 10]. A second diagnostic neutral beam is used for CHERS, this one injecting neutral hydrogen atoms [9]. Hydrogen atoms colliding with carbon impurities can exchange charge, passing off their electrons to the carbon, where they are left in an excited state. The carbon ions then emit photons as these electrons immediately drop to lower energy states. A spectrometer measures 343 nm emission from the C-VI transition, one of the brightest emission lines in MST [11]. The Doppler broadening of the line provides the ion temperature, and the Doppler shift of the line provides the ion flow velocity [12].

While the temperature of the bulk ions may be of more interest, the temperature of the carbon ions is correlated to the temperature of the deuterium ions, and the CHERS system has the major advantage of providing radial profiles of the temperature. A radial array of vacuum port windows provides views perpendicular to the neutral beam. Each port provides two views: one view on-beam and one view off-beam. Signal from the off-beam view is subtracted from signal from the on-beam view to remove background radiation. A fiber-optic bundle carries the light from one of these port windows to the two-channel spectrometer. Although only one spectrometer is available, the fiber-optic bundle can easily be moved from port to port throughout a run day, while the bulky neutral particle analyzers from the Rutherford scattering diagnostic are difficult to move an have poor radial resolution.

2.2.4 Electron Density: FIR Interferometry

Electron density is measured with a multichannel far-infrared (FIR) heterodyne interferometer system [13–15]. The index of refraction of a plasma is proportional to its electron density, thus the phase difference between a measurement beam passing though the plasma and a reference beam passing through vacuum is proportional to the line-averaged electron density [6]. The signal beam is split into eleven separate paths to provide eleven line-averaged measurements that can be inverted for a density profile. Six chords are offset 5° toroidally from the other five, providing toroidal information as well. Note that the FIR system doubles as a polarimeter, discussed in Sec. 2.3.3.

2.3 Equilibrium Reconstruction

Several diagnostics measure various aspects of the magnetohydrodynamic equilibrium in MST. All of this information is then used by the Grad-Shafranov solver MSTFit to produce a complete picture of the equilibrium, i.e., the magnetic and current density profiles of the plasma. The reconstructed equilibrium is used by CQL3D, as described in Chapter 4.

2.3.1 External Measurements

Many of the magnetic field and current measurements are made by a set of external diagnostics. In particular, the plasma current and poloidal shell currents are measured with Rogowski coils, while the total toroidal flux and loop voltage are measured with single turn loops. Magnetic modes are monitored by measuring fluctuations at the plasma boundary with a toroidal array of 64 magnetic pickup coil triplets and a poloidal array of 16 triplets.

2.3.2 Motional Stark Effect

While coils can measure average magnetic fields and fields at the plasma boundary, other diagnostics are required to measure the magnetic field in the core of the plasma. One such diagnostic is the motional Stark effect (MSE) system [8, 10]. The Stark effect refers to the splitting of spectral lines induced by an electric field, or in the case of the motional Stark effect, splitting induced by an atom traveling through a magnetic field, where $\boldsymbol{E} = \boldsymbol{v} \times \boldsymbol{B}$ [6]. Using the same hydrogen neutral beam as the CHERS system, the MSE diagnostic uses its own viewport and spectrometer to measure splitting of the Balmer-α line at 656.3 nm. For hydrogen atoms the splitting

is directly proportional to $|\boldsymbol{v} \times \boldsymbol{B}|$, and since $\boldsymbol{v}$ is well known from the properties of the neutral beam, $\boldsymbol{B}$ can then be found. The line of sight of the MSE viewport intersects the neutral beam at the magnetic axis, thus MSE provides a measurement of the field strength on axis.

2.3.3 Polarimetry

The FIR interferometer system doubles as a polarimetry diagnostic [15, 16]. The laser beams have a rotating elliptical polarization, which when passing through a polarizer at the end of the beam path produce amplitude-modulated beams for measurement. The phases between the measurement beam and reference beam are compared, with the difference being due to Faraday rotation in the plasma. The degree of Faraday rotation is directly proportional to the magnetic field strength in the direction of the beam [6]. This diagnostic thus provides a radially resolved measurement of the vertical field, which contains both toroidal and poloidal components.

2.3.4 MSTFit

The MHD equilibrium of MST is determined using MSTFit, a non-linear Grad-Shafranov toroidal equilibrium reconstruction code [17]. This code was written specifically for the equilibrium of an RFP with a close-fitting conducting shell at the boundary. An equilibrium is found that best fits all the available measured data from both the magnetic diagnostics described in this section and the pressure diagnostics described in the previous section. The results can be written to an EQDSK file compatible with those from tokamak equilibrium codes.

2.4 Soft-x-ray Tomography

X-ray emission has for several decades been used to monitor the dynamics of tearing modes in the RFP [18, 19]. On MST, soft x-ray tomography is used to study the magnetic topology of the plasma, as well as to infer 2D electron temperature profiles [20]. Tomographic data are gathered with four x-ray cameras at the same toroidal angle but at different poloidal angles. Each camera is comprised of an array of silicon photodiodes shielded by an aluminum housing with a pinhole covered with a beryllium filter, providing a total of 74 viewing chords [21]. The brightness measured by the 74 chords is inverted, providing a 2D profile of soft-x-ray emissivity. This inversion reveals nonaxisymmetric features in the plasma, such as magnetic islands [20]. One such example is shown in Fig. 2.3. Note that this is a separate diagnostic from the one described in the next chapter: it provides useful 2D information about the topology of the plasma, but the data are not spectrally resolved.

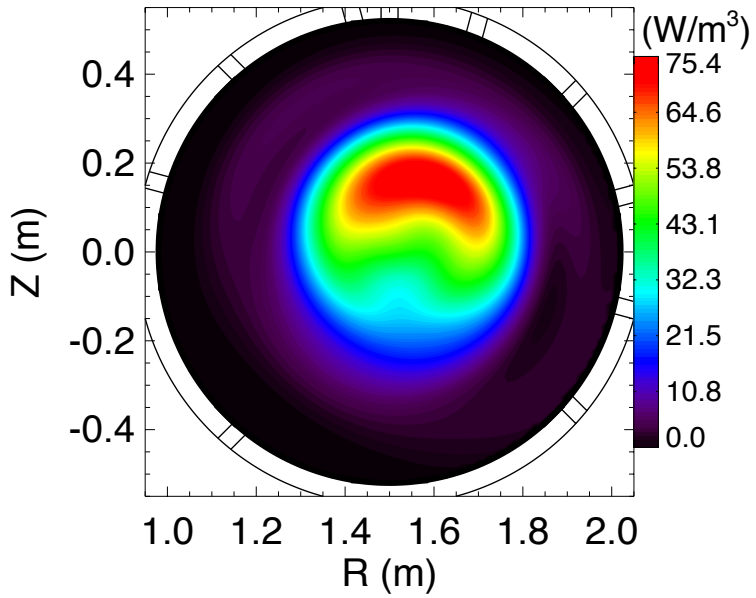

Figure 2.3: Example of an inverted sxr emissivity profile, revealing a large, asymmetric island structure in the core of an MST discharge.

References

[1] R. N. Dexter, D. W. Kerst, T. W. Lovell, S. C. Prager, and J. C. Sprott, Fusion Technol. **19**, 131 (1991).

[2] D. J. D. Hartog, N. Jiang, and W. R. Lempert, Rev. Sci. Instrum. **79**, 10E736 (2008).

[3] R. O'Connell, D. J. D. Hartog, M. T. Borchardt, D. J. Holly, J. A. Reusch, and H. D. Stephens, Rev. Sci. Instrum. **79**, 10E735 (2008).

[4] J. A. Reusch, M. T. Borchardt, D. J. D. Hartog, A. F. Falkowski, D. J. Holly, R. O'Connell, and H. D. Stephens, Rev. Sci. Instrum. **79**, 10E733 (2008).

[5] H. D. Stephens, M. T. Borchardt, D. J. D. Hartog, A. F. Falkowski, D. J. Holly, R. O'Connell, and J. A. Reusch, Rev. Sci. Instrum. **79**, 10E734 (2008).

[6] I. H. Hutchinson, *Principles of Plasma Diagnostics*, Cambridge University Press, second edition (2002).

[7] J. C. Reardon, G. Fiksel, C. B. Forest, A. F. Abdrashitov, V. I. Davydenko, A. A. Ivanov, S. A. Korepanov, S. V. Murakhtin, and G. I. Shulzhenko, Rev. Sci. Instrum. **72**, 598 (2001).

[8] D. J. D. Hartog, D. Craig, D. A. Ennis, G. Fiksel, S. Gangadhara, D. J. Holly, J. C. Reardon, V. I. Davydenko, A. A. Ivanov, A. A. Lizunov, M. G. O'Mullane, and H. P. Summers, Rev. Sci. Instrum. **77**, 10F122 (2006).

[9] G. F. Abdrashitov, V. I. Davydenko, P. P. Deichuli, D. J. D. Hartog, G. Fiksel, A. A. Ivanov, S. A. Korepanov, S. V. Murakhtin, and G. I. Shulzhenko, Rev. Sci. Instrum. **72**, 594 (2001).

[10] D. Craig, D. J. D. Hartog, G. Fiksel, V. I. Davydenko, and A. A. Ivanov, Rev. Sci. Instrum. **72**, 1008 (2001).

[11] D. Craig, D. J. D. Hartog, D. A. Ennis, S. Gangadhara, and D. Holly, Rev. Sci. Instrum. **78**, 013103 (2007).

[12] S. Gangadhara, D. Craig, D. A. Ennis, and D. J. D. Hartog, Rev. Sci. Instrum. **77**, 10F109 (2006).

[13] S. R. Burns, W. A. Peebles, D. Holly, and T. Lovell, Rev. Sci. Instrum. **63**, 4993 (1992).

[14] Y. Jiang, D. L. Brower, and N. E. Lanier, Rev. Sci. Instrum. **70**, 703 (1999).

[15] D. L. Brower, Y. Jiang, W. X. Ding, S. D. Terry, N. E. Lanier, J. K. Anderson, C. B. Forest, and D. Holly, Rev. Sci. Instrum. **72**, 1077 (2001).

[16] N. E. Lanier, J. K. Anderson, C. B. Forest, D. Holly, Y. Jiang, and D. L. Brower, Rev. Sci. Instrum. **70**, 718 (1999).

[17] J. K. Anderson, C. B. Forest, T. M. Biewer, J. S. Sarff, and J. C. Wright, Nucl. Fusion **44**, 162 (2004).

[18] G. A. Wurden, Phys. Fluids **27**, 551 (1984).

[19] R. J. Hayden and B. Alper, Plasma Phys. Control. Fusion **31**, 193 (1989).

[20] P. Franz, L. Marrelli, P. Piovesan, I. Predebon, F. Bonomo, L. Frassinetti, P. Martin, G. Spizzo, B. E. Chapman, D. Craig, and J. S. Sarff, Phys. Plasmas **13**, 012510 (2006).

[21] P. Franz, G. Gadani, R. Pasqualotto, L. Marrelli, P. Martin, G. Spizzo, P. Brunsell, B. E. Chapman, F. Paganucci, P. Rossetti, and C. Xiao, Rev. Sci. Instrum. **74**, 2152 (2003).

Chapter 3

The X-ray Spectroscopy Diagnostic

X-ray detectors were one of the earliest diagnostics used to study plasmas in fusion devices. For example, as far back as the 1950s, an x-ray detector was used to measure emission from runaway electrons striking the wall of the B-1 stellerator [1]. Most of these early diagnostics employed scintillators and photomultiplier tubes to detect x-rays. However, recent developments with semiconductor photodiode detectors have produced x-ray detectors with far better energy resolution, as x-ray energy is converted directly into a measurable current [2]. With these detectors, electrodes are placed on either side of a semiconducting crystal, and a large bias voltage is applied. When ionizing radiation strikes the crystal, electron-hole pairs are created; the electrons are collected by the anode and the holes by the cathode. The number of electron-hole pairs freed is proportional to the energy of the incident photon, thus the charge collected by the electrodes is directly proportional to x-ray energy. For CdZnTe detectors, an electron-hole pair is created for every 4.64 eV of energy deposited by the x ray; for silicon detectors it is 3.62 eV.

The design of the x-ray spectroscopy system on MST is loosely based on a similar diagnostic on TORE SUPRA, which employs two CdTe hard-x-ray cameras [3]. CdTe

and CdZnTe detectors have several advantages over earlier types of hxr semiconductor detectors, such as germanium detectors. These advantages include a faster response time and the ability to operate at room temperature. While similar diagnostics have been used on other plasma devices, the MST x-ray spectroscopy diagnostic is the first of its kind to be installed on a reversed-field pinch.

3.1 The X-ray Detectors

Rather than using x-ray cameras with arrays of detector crystals, the diagnostic on MST utilizes an array of separate, single-crystal detectors, with each detector installed on its own port window. A major advantage of this system is its flexibility; for instance, each detector can have different sized apertures and filters. One disadvantage is that a large number of vacuum ports are required; however, these ports are available on MST. The diagnostic currently consists of 18 detectors that can be placed on any of the 25 available x-ray ports. Twelve of these detectors have CdZnTe crystals and were designed to measure 10–300 keV x rays, and six have Si photodiodes and are optimized for 2–10 keV x rays.

Each photodiode detector is packaged with a charge sensitive preamplifier. The preamplifier circuit is essentially a current-to-voltage converter, outputting a voltage pulse with an amplitude proportional to the amount of charge collected each time an x ray strikes the photodiode. A simplified version of this circuit is depicted in Fig. 3.1. The output of each photodiode/preamp unit is then sent though a shaping amplifier, which amplifies the magnitude of these pulses, reduces the noise of the signal, and provides a quickly restored baseline to allow for higher counting rates. For this diagnostic, Gaussian shaping amplifiers were selected to provide pulses that are

easily fit after digitization, as described in Sec. 3.3.2.

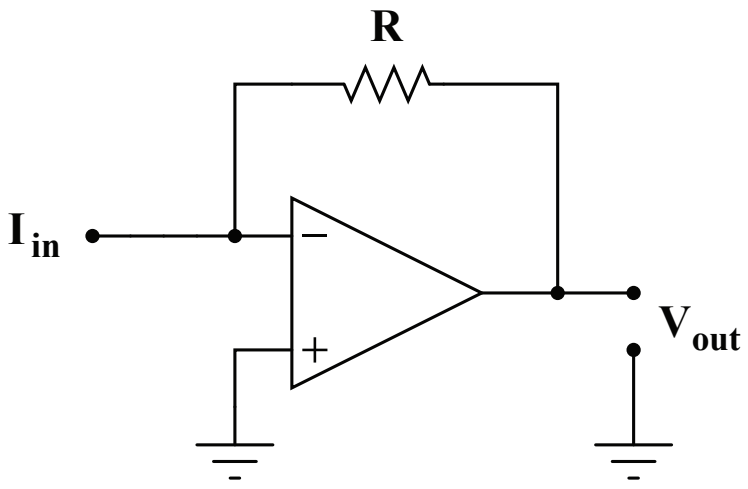

Figure 3.1: A simplified circuit diagram of a charge sensitive preamplifier, where $V_{out} = -I_{in}R$.

3.1.1 CdZnTe Hard-X-Ray Detectors

The x-ray spectroscopy diagnostic was initially designed around a set of CdZnTe photodiode detectors custom built for MST by eV Products (now EI Detection & Imaging Systems, a division of Endicott Interconnect Technologies, Inc.) [4]. The set consisted of 16 individually packaged detectors, of which 12 are still operational today. Each photodiode uses a $10 \times 10 \times 2$ mm CdZnTe crystal, which is thinner than those found in most off-the-shelf detectors. The thinner crystals provide better energy resolution, but begin to lose efficiency at energies above 300 keV. X-rays detected in MST are lower energy (< 150 keV) than in most applications using CdZnTe detectors, and the detection efficiency in this energy range is near unity for these crystals. Each

photodiode is packaged with a preamplifier, making the total unit $52 \times 20 \times 14$ mm. The anodized aluminum case has a 12.5×12.5 mm Mylar window, and has been partially removed to show the interior in Fig. 3.2. This window, together with a thin aluminum window or transmission filter, block most photons with energies less than 10 keV.

Figure 3.2: A CdZnTe hxr detector from eV Products with the cover removed.

Included in the eV Products system is a power supply that provides the bias voltage and preamp power for each detector, and a box with 16 Gaussian shaping amplifiers. The heights of the Gaussian pulses are proportional to x-ray energy and the gain can be adjusted to produce pulse heights appropriate for the ± 5 V digitizer inputs. The full width at half of the maximum height (FWHM) of a pulse is fixed by the shaping amplifiers to be about 1.2 μs.

3.1.2 Si Soft-X-Ray Detectors

A new XR-100CR detector from Amptek Inc. is used to measure lower energy x-rays. This silicon soft-x-ray detector operates in much the same way as its CdZnTe counterparts, but is most effective at x-ray energies below 10 keV, with a detector efficiency near unity in this range. Five more of these off-the-shelf detectors are currently being added to the diagnostic to provide a radial profile of measurements at these energies. Each detector package consists of a Si photodiode, charge-sensitive preamplifier, and thermoelectric cooler with a temperature monitor to regulate the photodiode's temperature. The detector crystal measures $5.0 \times 5.0 \times 0.5$ mm, and the total package is $83 \times 57 \times 28$ mm. Each unit has a 25 μm beryllium window, which in addition to the 150 μm beryllium vacuum windows installed on MST blocks most x-rays with energies less than 2 keV. The detector unit is shown in Fig. 3.3.

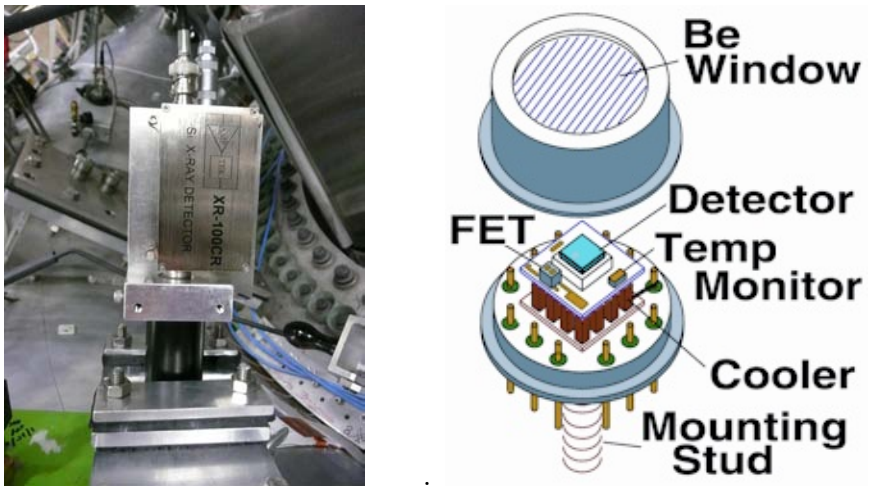

Figure 3.3: A photo of an Amptek XR-100CR mounted on MST, and a drawing of the detector from the product website.

Amptek's PC5 power boards provide the bias voltage, preamplifier power, and

thermoelectric cooling power for each soft-x-ray detector. The shaping amplifiers used with these detectors are from Cremat, Inc. As with the shaping amplifiers from eV Products, these amplifiers create Gaussian pulses with pulse heights proportional to x-ray energy and adjustable gains. Two sets of amplifiers with different shaping times are used. One set provides pulses with FWHM of 1.2 μs, similar to the eV Products amplifiers, and the other set provides pulses with FWHM of 240 ns, for better time resolution.

3.2 Detector Installation

Advantages of using small photodiode detectors are that they are relatively easy to mount on the machine, easy to move, and can fit in tight spaces. Twenty-five x-ray windows are currently installed on MST, and the detectors can be moved from one window to another in a matter of minutes.

3.2.1 Distribution of the Detectors

The majority of the x-ray detectors are distributed along a radial array of seventeen vacuum ports. Thirteen of these ports form the "boxport," in which a large, rectangular, aluminum flange covers thirteen 1.25 inch holes in the vacuum vessel, arranged in a row and spaced 2 inches apart. A hole has been drilled into the boxport flange above each hole in the vacuum vessel, and an NW-25 quick release (KF) flange is welded into each. The boxport is located at 150° toroidal on the vacuum vessel and the lines of sight of each port make a 67.5° angle with the midplane. The sixth port in from the outboard side views the approximate location of the Shafranov-shifted magnetic axis, 6 cm outboard of the geometric axis. The boxport covers a radial range of

roughly $r/a = \pm 0.6$.

To extend the radial range of the diagnostic, four more "edge ports" have been added, two on either side of the boxport. The seventeen ports that form the radial array are shown in Fig. 3.4. The locations of the edge ports, as well as additional, toroidally displaced ports with x-ray windows, are listed in Table 3.1. Each of these ports has an NW-40 KF flange, which are larger than those used on the boxport (inner diameter of 40 mm versus 25 mm).

3.2.2 Mounting the Detectors

An x-ray vacuum window is placed on each port. Until recently, these were aluminum KF stubs, each with a 0.5 inch hole drilled most of the way through, leaving 400 μm of aluminum to act as the window. These have since been replaced with new windows to allow transmission of soft x rays. The new windows consist of 150 μm thick, 0.62 inch diameter beryllium disks vacuum brazed onto stainless steel KF stubs with 0.5 inch holes drilled through them. The transmission of these windows is described in more detail in Sec. 3.4.2.

The detectors are mounted over the x-ray windows using specially designed hardware as shown in Fig. 3.5. Several features of the detector mounts were implemented to reduce noise and extraneous radiation pickup. Two large sources of electronic noise have been discovered, primarily through experimental trial and error, and have been mostly eliminated. The first source of noise was noticed to be due to mechanical vibrations. This problem is particularly pronounced with the CdZnTe detectors. During a plasma discharge, the MST vacuum vessel shakes violently. It was discovered that a detector lying on top of the vacuum vessel, separated only by a thin sheet of electri-

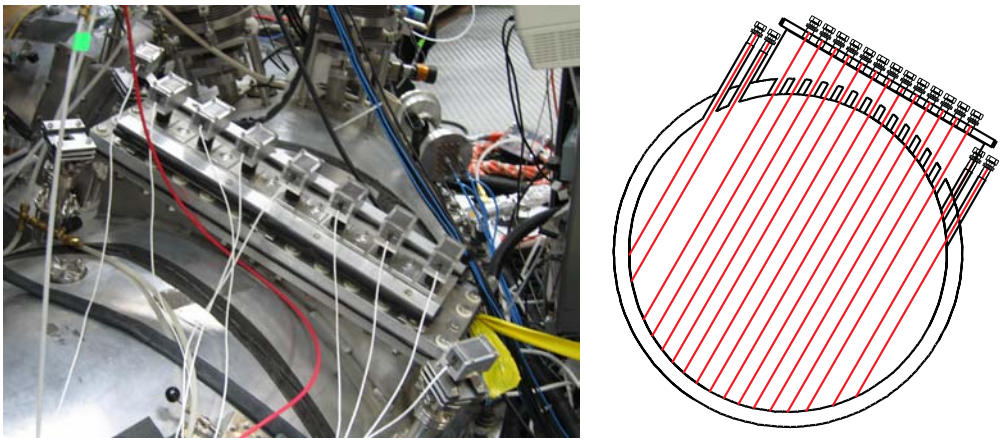

Figure 3.4: A photo of the boxport and nearby edge ports, and a drawing of the lines of sight of each.

Tor. Angle	Pol. Angle	r/a	Port Dia.	Notes
60.0°	75.0°	0.111†	1.5 in.	
90.0°	123.2°	0.564	1.25 in.	above LH antenna
90.0°	157.5°	0.000	2.0 in.	above LH antenna
105.0°	75.0°	0.111†	1.5 in.	
120.0°	75.0°	0.111†	1.5 in.	
140.0°	90.0°	0.000	1.5 in.	above EBW antenna
145.0°	112.3°	-0.772	1.25 in.	edge port
145.0°	17.5°	0.840	1.25 in.	edge port
155.0°	120.1°	-0.871	1.25 in.	edge port
155.0°	26.6°	0.718	1.25 in.	edge port
180.0°	135.0°	0.082†	1.5 in.	views target probe
240.0°	135.0°	0.082†	1.5 in.	alternate for target probe

Table 3.1: The positions of the x-ray ports with NW-40 flanges (spring 2010). r/a is the shortest distance between the line of sight and the geometric axis, divided by the minor radius (0.52 cm). A negative number indicates the view is inboard of the axis. A dagger (†) indicates the view is through the magnetic axis, shifted 6 cm outboard of the geometric axis.

cally insulating material, exhibited much more noise than a detector separated from the machine by a vibration-damping material. To solve this problem, every detector is now mechanically isolated from the vessel by Sorbothane, a synthetic polymer known for its shock and vibration damping properties.

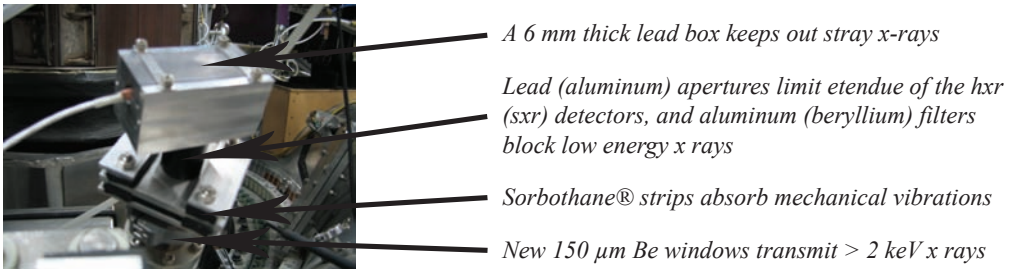

Figure 3.5: HXR detector mounting assembly.

The second source of noise is radio-frequency pickup. The Si detectors in particular are constructed with poor shielding, not being designed for an environment with large amounts of electromagnetic noise, as is the case near MST during a plasma discharge. Noise in the detector signals has been greatly reduced simply by wrapping the detector/preamp units with aluminum foil or conducting tape.

Finally, in the early days of operation, it was noticed that more high-energy x-rays were detected than expected when compared to lower energy flux. It was soon discovered that this was due to high energy flux penetrating the 5 cm thick aluminum vacuum vessel and striking the detector crystal from outside the expected viewing angle. This problem has been solved by enclosing the detectors in 6 mm thick lead boxes, which block all but one in 1×10^{10} 150 keV x-rays.

3.3 Signal Processing

Most spectroscopy systems utilizing semiconductor detectors and shaping amplifiers use multichannel analyzers (MCAs) to separate pulses by height into various energy channels. The counts in each channel can be used to compute an energy spectra. While this is sufficient for most applications, the fast dynamic processes in a device such as MST can be better studied if the arrival time of each pulse is also recorded. Therefore, the signals from each detector on MST are digitized and processed by a user-written code. Besides giving a time stamp to each pulse, this has several other benefits over a conventional MCA. Pulses can be sorted into useful time and energy bins at any time after the data is collected. Other advantages include the ability to separate Gaussian pulses from noise and identifying, and possibly resolving, pileup of pulses.

3.3.1 Digitization of the Signals

The data collection electronics are installed in a crate with a VME bus. The data presented in subsequent chapters was recorded with two Hytec VTR 2535W 8-channel VME analog-to-digital converters. These digitizers convert $\pm$5V input signals into 12-bit, 10 megasample per second digital data. Each channel can store up to 524 kilosamples per discharge. These digitizers were controlled by a VMIC VMIVME-7750 Pentium III processor-based VME single board computer. The digitizers are currently being replaced by three Struck SIS3302 8-channel VME ACDs. Each channel has 16-bit resolution and can record 100 megasamples per second, storing 32 megasamples per channel. Besides providing additional channels to accommodate the new sxr array, these new digitizers will allow fitting to the faster 240 ns Cremat shaping amplifier

pulses, as several data points per pulse are required to fit a proper Gaussian. The VME controller is being replaced by a Struck SIS3150-USB, a USB to VME interface that will allow control of the crate by a regular desktop computer.

All channels receive a trigger 0.01 ms before the beginning of an MST discharge, though this can easily be varied. The Hytec digitizers can store data for 52 ms, which includes most of the discharge and misses only the end of the current ramp-down stage. The Struck digitizers will record an entire discharge.

3.3.2 Pulse Fitting

Once the digitized signal is stored and transfered to a hard drive, a fitting routine is used to pick out Gaussian pulses and record their heights and times. A least squares fit of a Gaussian of fixed width (determined by the shaping amplifier) is performed on all ranges of the data that exceed the noise floor. The heights and times of well-fit pulses are saved, and poorly-fit pulses can be rejected, or an attempt to fit two overlapping Gaussians can be made. If a two-Gaussian fit also fails, the pulse is rejected as noise, though this is also recorded so that the user may determine the quality of the final data set. Fig 3.6(a) shows an example of a digitized signal, and Fig 3.6(b) shows an example of a pulse fit, calibrated as described in the next section.

3.3.3 Energy Calibration

Calibration is performed with known x-ray sources. Iron-55 is used to calibrate the sxr detectors and Americium-241 the hxr detectors. Iron-55 decays via electron capture to manganese-55, and an outer shell electron drops into the vacated lower-energy orbit, emitting a K-alpha x ray at 5.9 keV. Americium decays via alpha emission

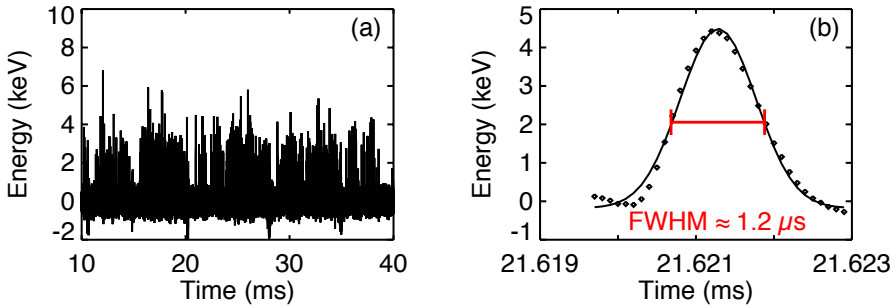

Figure 3.6: (a) Calibrated signal from the Si detector, where each spike is a Gaussian pulse representing one measured x ray. (b) Closeup of a pulse at 21.6213 ms, fit with a fixed-width Gaussian. It is found to have an energy of 4.67 keV.

to neptunium-237, emitting a 59.5 keV x-ray in the process.

Before calibration, the voltage gain on each shaping amplifier is adjusted to fully utilize the 5 V range of the digitizers. For the sxr detectors, the 5.9 keV pulses are set just under 3 V so that the maximum energy of interest (10 keV) is just under 5 V. With the hxr detectors, the 59.5 keV pulses are set just under 1.5 V so that the maximum energy of interest (200 keV) is just under 5V. Thousands of these pulses are then fit with Gaussians, and the mean and standard deviation of all the measured pulse heights provide the proper bit value to x-ray energy conversion and the error in the measurement, or energy resolution. Typical errors are 450 eV for the sxr detectors and 2 keV for the hxr detectors.

A sample calibration of an hxr detector with the Am-241 source is shown in Fig. 3.7. In this example, 28,557 pulses are fit with Gaussians, and the pulses are then binned by the heights of the Gaussians, which are in units of bits. The result is

then fit with a Gaussian, where the center represents the calibration and the width provides the measurement error. In this case, the center is at about 606 bits, thus 606 bits = 59.5 keV. The error in the measurement is

$$16.68 \text{ bits} \times \frac{59.5 \text{ keV}}{606 \text{ bits}} = 1.64 \text{ keV}. \tag{3.1}$$

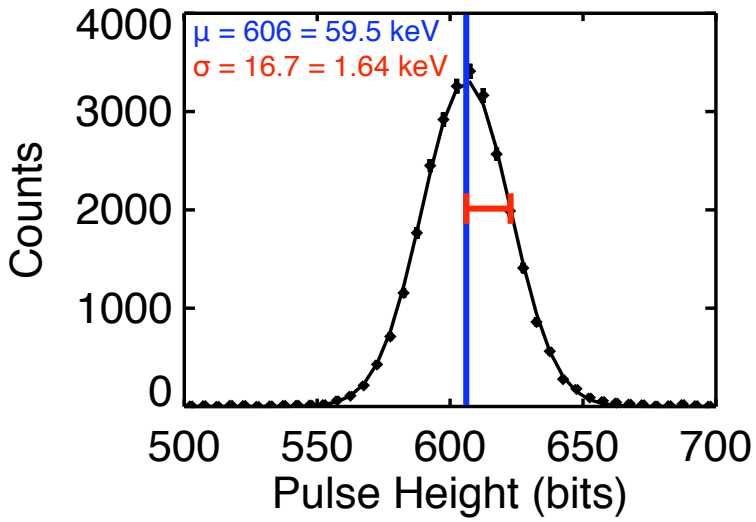

Figure 3.7: The average pulse height when measuring an Am-241 source is calibrated to 59.5 keV. The standard deviation of the pulse heights represents the broadening of the spectral line due to measurement errors.

Once this is complete, an energy can be assigned to every pulse measured during a plasma discharge. The final output of the fitting program is an array that assigns a time, energy, and detector number to every x-ray measured.

3.4 Calculating Energy Flux and Spectra

After the pulses are fit and calibrated, they can be binned by time and energy to produce spectra. Because the diagnostic measures individual x-rays, the primary source of uncertainty in the resulting spectra is the finite count rate. Since the relative error of each bin goes as $1/\sqrt{n}$, where n is the number of counts, a larger x-ray count means less error, or better resolution (more bins can be used). Since only continuous emission is of interest with this diagnostic, usually about 100 counts are enough to provide an adequate spectrum.

Once the calibrated energies of the pulses are summed together in each bin, the resulting data represent the total energy collected by each detector in each time and energy window. This data must then be normalized if it is to be compared to data from other discharges, other experiments, or numerical simulations. Bin size, detector geometry, and filter transmission must be considered. The first step, normalizing by bin size, is quite simple. Each bin is divided by its width in both time and energy. The result is can be expressed in units of $\text{ergs} \cdot \text{s}^{-1} \cdot \text{keV}^{-1}$.

3.4.1 Apertures and Etendue

The data now has the form of the total power collected by a detector as a function of time and energy. This power depends on the detector's area and the solid angle it views, and can be written as $I(\nu)A_d\Omega_d$, where $I(\nu)$ is the intensity, or energy flux, of interest, A_d is the area of the detector, and Ω_d is the solid angle it views. The total power comes from the light emitted by the plasma volume seen by the detector along its line of sight s:

$$I(\nu)A_d\Omega_d = \int j(\nu, s)A_p\Omega_p \, \mathrm{d}s, \tag{3.2}$$

where j is the plasma emissivity, as described by Eq. 1.8. The quantities A_d, A_p, Ω_d, and Ω_p are the areas and solid angles shown in Fig. 3.8(a). A solid angle is just the area of a segment of a unit sphere, so $\Omega_d = A_p/4\pi r^2$ and $\Omega_p = A_d/4\pi r^2$, where r is the distance between the detector and the plasma volume element. Since r is the same both cases, $G \equiv A_d\Omega_d = A_p\Omega_p$, where G is the detector etendue. Etendue is a constant that can be removed from the integral, thus Eq. 3.2 becomes

$$I(\nu) = \int j(\nu, s) \, \mathrm{d}s. \tag{3.3}$$

The energy flux $I(\nu)$ is thus independent of the detector geometry can be found by dividing the measured power by the setendue.

The etendue is determined by a set of two apertures, which are used to limit the x-ray flux that reaches a detector to prevent pulse pileup. Depending on plasma conditions, x-ray flux can vary by many orders of magnitude, thus several aperture sizes and configurations are needed to prevent pileup while still allowing enough flux through for an accurate measurement. For the soft-x-ray detectors, two 6 mm thick aluminum disks with holes of diameter d_1 and d_2 are placed in an optical tube of length l, as shown in Fig. 3.8(b). A 6 mm thick aluminum tube spacer is placed inside the optical tube between the two apertures. Aluminum of this thickness blocks virtually all 10 keV x rays. In the case of the hard-x-ray detectors, lead is used in place of the aluminum: 6 mm of lead blocks almost all x rays with energies less than 150 keV. Transmission of x rays through solid materials is discussed in more detail in the next

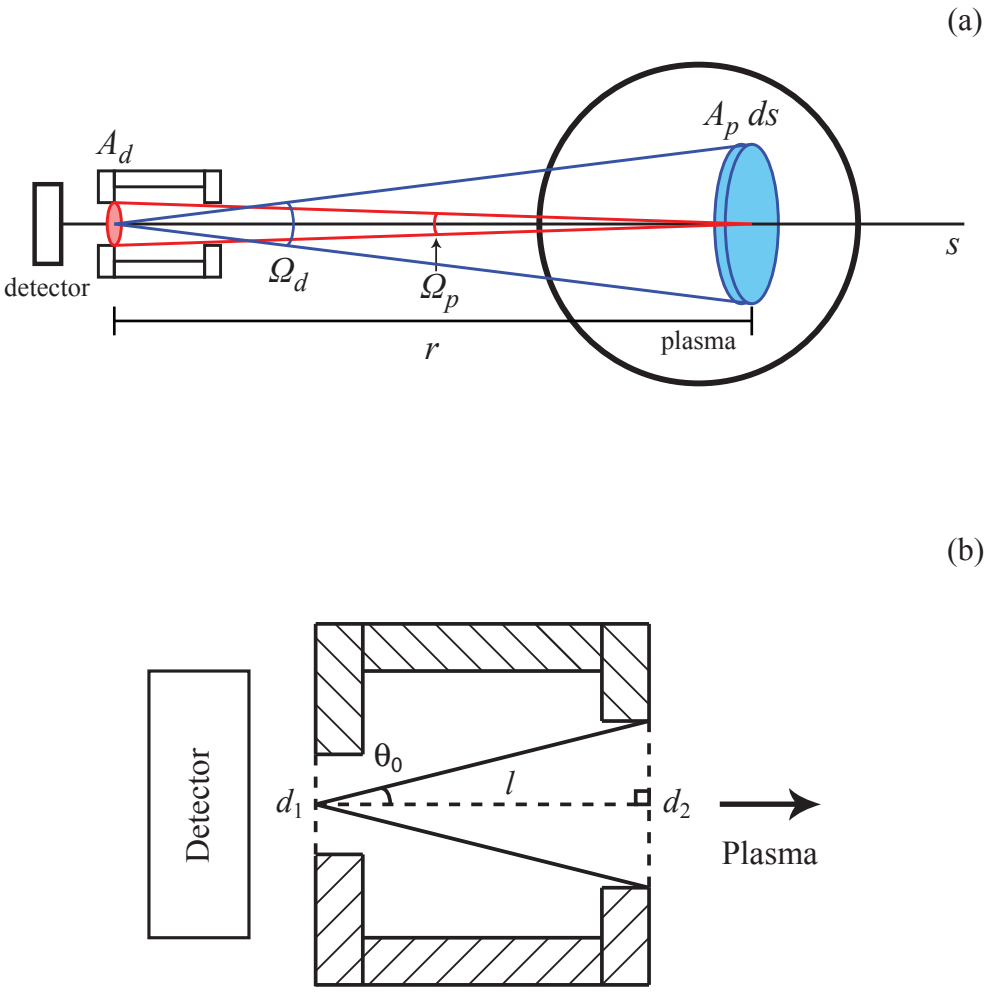

Figure 3.8: (a) The detector geometry, with the blue lines representing the solid angle through which a point on the detector views the plasma, and the red lines representing the solid angle through which a plasma volume element emits light that is picked up by the detector. (b) A close-up of the apertures. The hatching lines represent aluminum (for sxr detectors) or lead (for hxr detectors) apertures and spacer. Note that this figure is not to scale, as typically $d_1, d_2 \ll l$.

section.

The area of the entrance aperture is simply

$$A_d = \frac{\pi}{4} {d_1}^2, \tag{3.4}$$

while the solid angle measured by the detector depends on the diameter of the second aperture, which is closest to the plasma:

$$\Omega_d = \int_0^{2\pi} \int_0^{\theta_0} \sin\theta \; \mathrm{d}\theta \; \mathrm{d}\phi = 2\pi(1 - \cos\theta_0). \tag{3.5}$$

From the aperture geometry, shown in Fig. 3.8(b),

$$\cos\theta_0 = \frac{l}{\sqrt{l^2 + {d_2}^2/4}}. \tag{3.6}$$

Subbing Eq. 3.6 into Eq. 3.5 and multiplying it with the area found in Eq. 3.4, the etendue of a detector is

$$G = \frac{\pi^2 {d_1}^2}{2} \left(1 - \frac{l}{\sqrt{l^2 + {d_2}^2/4}} \right). \tag{3.7}$$

It should be noted that apertures are typically chosen small enough so that they are the limiting factor of the solid angle viewed by each detector; that is, the detector's view through the apertures is not obstructed by vacuum hardware or the inside wall of the vacuum port. This provides an easy and well known measurement of each detector's etendue. A list of standardized aperture configurations is provided in Table 3.2. Due to difficulties in machining lead, the smallest aperture size used with the hxr detectors is 0.10 in., while aluminum apertures with a diameter of 0.05 in. are used with the sxr detectors.

Aperture Set	d_1 (in.)	d_2 (in.)	l (in.)	$G(\mathrm{cm}^2 \cdot \mathrm{sr})$	Relative G
HXR 1, SXR 1	0.15	0.15	2.0	7.80×10^{-5}	1.0000
HXR 2, SXR 2	0.10	0.10	2.0	1.54×10^{-5}	0.1976
HXR 3	0.10	0.10	4.0	3.85×10^{-6}	0.0494
SXR 3	0.10	0.05	2.0	3.85×10^{-6}	0.0494
SXR 4	0.05	0.05	2.0	9.64×10^{-7}	0.0124
SXR 5	0.05	0.05	4.0	2.41×10^{-7}	0.0031

Table 3.2: Standard sets of apertures. The HXR sets are made from 6 mm thick lead, the SXR sets from 6 mm thick aluminum. Relative G is the ratio of the etendue to the etendue of the largest set.

The binned flux data are divided by etendue to provide fluxes that are independent of detector geometry, and can be expressed in units of $\mathrm{ergs} \cdot \mathrm{cm}^{-2} \cdot \mathrm{sr}^{-1} \cdot \mathrm{s}^{-1} \cdot \mathrm{keV}^{-1}$.

3.4.2 Filters and Transmission

All materials attenuate x-ray flux passing through them, and this must be accounted for when measuring x-ray spectra. The vacuum windows slightly attenuate x-ray flux, and filters are sometimes used to block out lower energy photons in favor of measuring higher energy x rays. Apertures and detector shields are chosen to block virtually all photons originating from outside of the desired view. X-ray flux decreases exponentially as it passes through a material, and the transmission of x-rays through a slab of material with thickness t is

$$T = e^{-\mu t}, \tag{3.8}$$

where the percentage of photons transmitted through the material is $T \times 100\%$ and $\mu = \mu(E)$ is the x-ray mass attenuation coefficient for a given material and depends

on x-ray energy E.

To accommodate the new sxr detectors, the aluminum windows have been replaced with 150 μm thick beryllium windows. To prevent detector saturation by low energy x rays, 300 μm and 1 mm beryllium filters can additionally be placed over the windows. To use the hxr detectors with the beryllium windows, aluminum filters must be used. 250 μm, 400 μm, and 4 mm aluminum filters are available. The 400 μm aluminum filters match the thickness of the old aluminum windows. The 250 μm filters were chosen to allow a larger flux of 10 keV x-ray through to the hxr detectors, while the 4 mm filters were chosen to block lower energy photons to allow better measurement of x-rays greater than 30 keV. Transmission curves of all of these filters are shown in Figs. 3.9, 3.10, and 3.11.

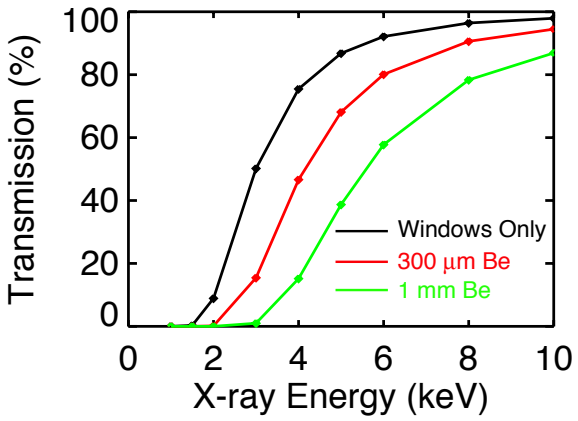

Figure 3.9: Percentage of flux that passes through a Be window, Be filter, and Be detector window as a function of energy. These filters are used with sxr detectors.

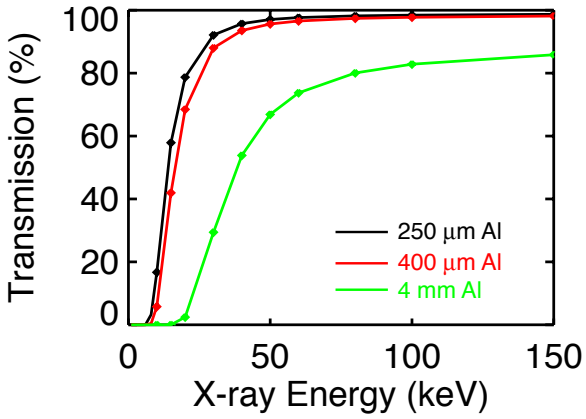

Figure 3.10: Percentage of flux that passes through a Be vacuum window and Al filter as a function of energy. These filters are used with hxr detectors.

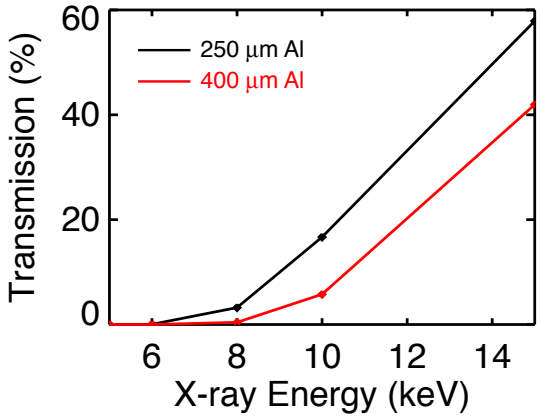

Figure 3.11: A closeup of Fig. 3.10 comparing the 250 µm Al filter to the 400 µm filter near 10 keV.

To recover the actual x-ray flux from the data, each bin must be divided by the average transmission of that bin. For example, the transmission of 6 keV photons through the 150 μm beryllium vacuum window, the 300 μm beryllium filter, and the 25 μm beryllium detector window is approximately 80%. Thus, for every four x rays detected in a 5.5–6.5 keV bin, it is assumed that one is blocked by the filters. Thus, dividing the total flux measured in this bin by 0.8 will correct for these blocked x rays. Clearly, since transmission is a function of energy, the energy bins must be narrow enough to have a well-defined transmission, but wide enough for good statistics. For data that are presented as a sum over all energies, the pulses were first separated into small energy bins, each bin was divided by the appropriate transmission, and then the bins were summed together. This final normalization does not change the dimensions of the data, and the final result can still be expressed in units of $\mathrm{ergs} \cdot \mathrm{cm}^{-2} \cdot \mathrm{sr}^{-1} \cdot \mathrm{s}^{-1} \cdot \mathrm{keV}^{-1}$. These are the units used throughout most of this thesis. An example of a spectrum using these units is shown in Fig. 3.12.

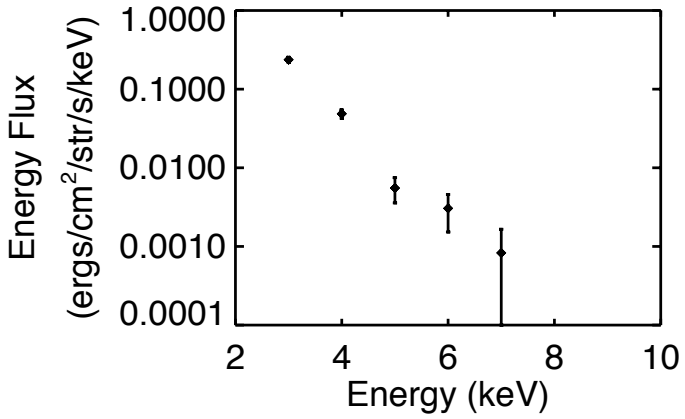

Figure 3.12: The spectrum found from the raw data shown in Fig. 3.6.

References

[1] W. Bernstein, F. F. Chen, M. A. Heald, and A. Z. Kranz, Phys. Fluids **1**, 430 (1958).

[2] Y. Eisen, A. Shor, and I. Mardor, Nucl. Instr. and Meth. A **428**, 158 (1999).

[3] Y. Peysson and F. Imbeaux, Rev. Sci. Instrum. **70**, 3987 (1999).

[4] R. O'Connell, D. J. D. Hartog, C. B. Forest, and R. W. Harvey, Rev. Sci. Instrum. **74**, 2001 (2003).

Chapter 4

Improved Confinement with Current Profile Modification

4.1 Introduction

One route to globally improved confinement in the RFP is through current profile modification via some form of auxiliary current drive. Magnetohydrodynamic modeling has shown that a reduction in the current gradient in the edge of an RFP can reduce the amplitudes of the core-resonant tearing modes driven by this gradient [1]. If reduced enough, the islands generated by these tearing modes should no longer overlap in the core of the plasma, and flux surfaces would be restored. The reduction of tearing modes has indeed been accomplished in MST and other RFPs through the use of pulsed parallel (poloidal) current drive (PPCD), where current is ohmically driven in the edge of the plasma to reduce the current gradient and thus reduce the free energy source of the tearing modes [2, 3]. Measurements have shown that PPCD essentially eliminates the $\langle \tilde{v} \times \tilde{b} \rangle$ mean-field emf by creating enough of an electric field to balance a simplified Ohm's law $E_{\|} = \eta J_{\|}$ [4, 5]. Modifications to the PPCD cir-

cuitry over the years have greatly improved its performance and extended its duration [6–8]. To date, MST discharges with PPCD have reached ion temperatures greater than 1 keV, electron temperatures of about 2 keV, and energy confinement times up to 12 ms [9]. When combined with pellet injection, MST has reached a total beta of 26%. All of these values are records for the RFP.

When PPCD is applied during an MST discharge, x rays with energies up to 150 keV are detected. The parallel electric field $E_{||}$ is actually reduced in the core during PPCD [5], thus the drastic increase in the runaway population must be due to a decrease in radial diffusion. Indeed, modeling with the Fokker-Planck code CQL3D [10] reveals that the radial diffusion of runaway electrons becomes independent of electron velocity, indicative of closed flux surface restoration. This code has been used to analyze data from fully diagnosed PPCD discharges to infer both the radial diffusion rate D_r and the effective ionic charge of the plasma Z_{eff}, a quantity not otherwise measured in MST. X-ray spectroscopy thus provides strong evidence of reduced stochasticity and improved particle confinement in an RFP when the current profile is sufficiently modified.

4.2 X-ray Observations During PPCD

Hard-x-ray flux is detected from the beginning of PPCD until shortly after it ends. Most of the flux is generated in the core of the plasma, where closed flux surfaces are restored. The details of the hxr measurements during PPCD are described in the following sections.

4.2.1 Energy Spectrum

When no additional transmission filters are placed in front of the 400 μm thick aluminum vacuum windows, low energy (10–25 keV) x rays dominate the measured hard-x-ray energy spectra. Small apertures must be used to prevent amplifier saturation by these low energy x rays, thus too few pulses with energies > 25 keV are measured to obtain spectra at these higher energies. However, with thicker filters, spectra with energies up to 150 keV have been measured. Fig. 4.1 shows the line-integrated spectra measured by a sxr and hxr detector, each viewing the magnetic axis from different windows. Note that even the hottest PPCD discharges ($T_e \sim 2$ keV) would only produce a measurable x ray flux up to about 15 keV if their distribution functions were purely Maxwellian.

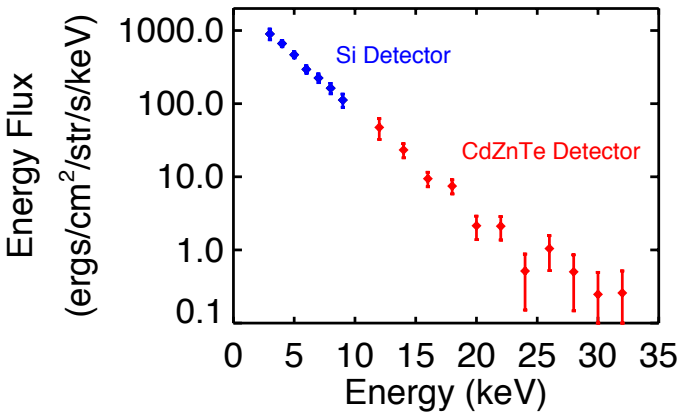

Figure 4.1: Spectra from a 500 kA PPCD discharge as measured by the sxr and an hxr detector viewing the core of the plasma.

4.2.2 Radial Profile

During PPCD, the hard-x-ray flux is largest within the core of the plasma, and drops drastically outside a radius of about $r/a = 0.5$, consistent with where closed flux surfaces are expected to form and the plasma is hottest. An example is shown in Fig. 4.2. The peak energy flux is shifted outboard due to the Shafranov shift of the magnetic axis. The profile is also asymmetric due to relativistic beaming of the bremsstrahlung emission.

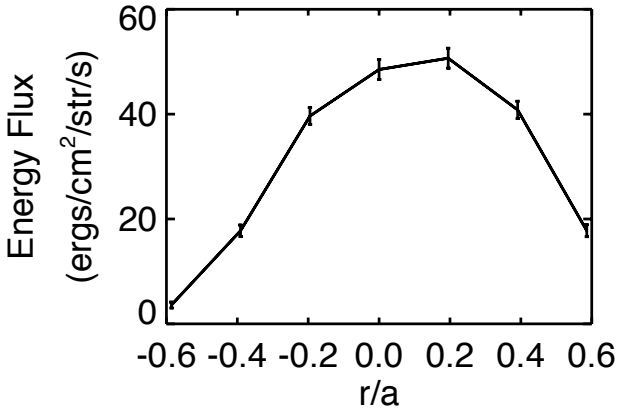

Figure 4.2: The radial profile of line-integrated hxr emission from a 500 kA PPCD discharge.

For a fast electron decelerated by a Coulomb collision, the distribution of radiated power is approximately

$$\frac{dP}{d\Omega} = \frac{\mu_0 e^2 a^2}{16\pi^2 c} \frac{\sin^2\theta}{(1-\beta\cos\theta)^5}, \tag{4.1}$$

where a is the acceleration (deceleration) of the electron, $\beta = v/c$, and θ is the

angle between electron velocity and the direction of the emission [11]. As an electron becomes relativistic, $\beta \rightarrow 1$ and the denominator grows very small for small values of θ. Thus relativistic electrons preferentially emit bremsstrahlung in the forward direction, and since electron current travels towards the outboard detectors and away from the inboard detectors, the flux is larger on the outboard side. This asymmetry is more pronounced at higher energies. When the direction of the poloidal magnetic field is reversed, reversing the direction of the electron current, the asymmetry also reverses, becoming larger on the inboard side, shown in Fig. 4.3.

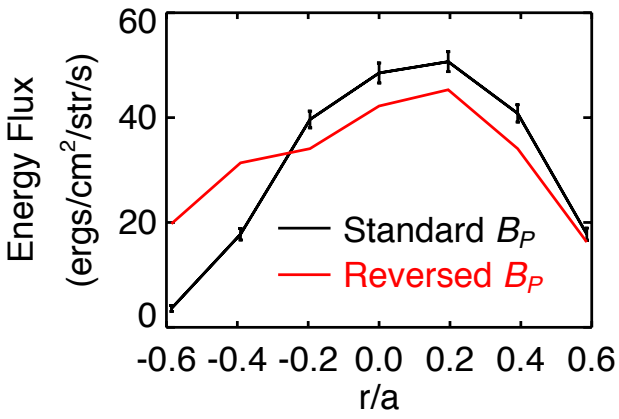

Figure 4.3: The flux is larger on the inboard side when B_P is reversed. Note that the values for the reversed case are only approximate and are scaled for comparison to the standard case, since the last time B_P was reversed for PPCD was before apertures were used with the detectors.

4.2.3 Time Evolution

At the start of PPCD, when the tearing modes are reduced and confinement begins to improve, the hard-x-ray flux increases exponentially in time. Fig 4.4 shows the flux initially growing fastest in the core (a), where the flux quickly saturates. At mid-radius (b), the flux grows more slowly, but eventually reaches a saturation level similar in magnitude to that of the core. When a sawtooth interrupts or ends PPCD, a small, short burst of x-rays is usually observed, most likely from fast electrons striking plasma limiters. After this burst, x-ray flux disappears completely within about 1 ms, the confinement time of a standard RFP plasma.

4.3 Finding D_r and Z_{eff} with Fokker-Planck Modeling

While the mere presence of hard x rays is a strong indicator of improved confinement, Fokker-Planck modeling can be used to quantitatively describe the radial diffusion of the runaway electrons.

4.3.1 The Fokker-Planck Code CQL3D

CQL3D, short for Collisional QuasiLinear 3D, is a three-dimensional, bounce-averaged, Fokker-Planck code. "The CQL3D code, which had its genesis in the CQL code [12], consists of a 2D-in-momentum-space, multi-species, relativistic, bounce-averaged, collisional/quasilinear FP equation solver running on a radial array of non-circular flux surfaces, in tandem with rf ray-tracing and/or neutral beam deposition packages [10]." While CQL3D was primarily written to model rf and neutral beam heating in tokamaks, it works equally well modeling radial transport in an RFP with globally improved confinement [13].

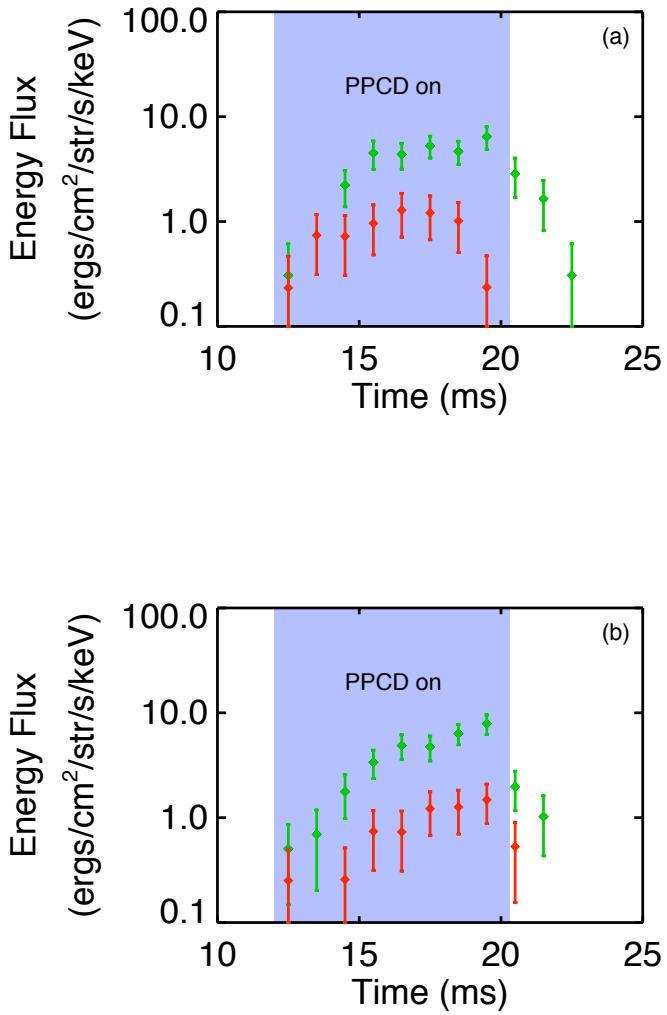

Figure 4.4: HXR flux as a function of time along lines of sight at (a) $r/a = 0.0$ and (b) $r/a = 0.39$. The green (larger valued) points represent flux from 12-20 keV x rays and the red (smaller valued) points show 20-28 keV x rays. The shaded region indicates the time during which magnetic mode activity is suppressed by PPCD.

6D phase space is reduced to 3D by assuming that the collision time is much greater than: (1) the time to reach equilibrium along a flux surface, eliminating the toroidal angle dependence of f_e; (2) the particle gyro time, eliminating the dependence on the azimuthal velocity angle about the field line; and (3) the particle bounce time, eliminating the poloidal angle dependence. This slow collision time assumption easily holds true for the fast electrons of interest. This leaves two momentum dimensions: $u = |p|/m$ and the pitch angle θ_0 between the momentum direction and the field line. The only remaining spatial dimension is the radial coordinate $\rho \equiv (\Phi/\pi B_{T0})^{1/2}$ (Φ is the toroidal flux through the surface and B_{T0} is the toroidal field at the major radius). Since the energy and magnetic moment of a particle are conserved, the pitch angle changes as the particle follows a field line and $|B|$ changes, so the pitch angle is defined at the point on the flux surface ρ where the magnetic field is at a minimum. Note that a "zero-banana-width" approximation is made (ρ is single-valued on a flux surface), there is only one local $|B|$ minimum per flux surface through which all particles pass, and the code assumes an up-down symmetry of the flux surface.

The bounce-averaged Fokker-Planck equation, which takes the form of the kinetic equation described in Chapter 1 (Eq. 1.10), is broken into six terms in the code: a relativistic Coulomb collision term, DC electric field term, RF quasilinear diffusion term, neutral beam source term, synchrotron radiation loss term, and a radial diffusion term. Balancing these six terms gives a steady-state, non-Maxwellian distribution function. The collisional term is a relativitstic version of the usual FP collision term with Rosenbluth potentials. The electric field term is simply $(q/m)\vec{E} \cdot \nabla_v f_e$. For the plasmas described in this chapter, no RF or neutral beam heating was used, though

others are using the code to study LH and EBW heating and current drive in MST, and it may be used in the future to study heating and current drive with a newly installed neutral beam injector. The synchrotron radiation term can also be ignored, as the power radiated by a 150 keV electron in a typical PPCD discharge is only

$$P = \frac{\mu_0 e^2 a^2 \gamma^4}{6\pi c} = 7.1 \times 10^{-16} \text{ W} = 4.4 \text{ keV/s}, \tag{4.2}$$

where a is the acceleration of the electron due to the centripetal force of the magnetic field [11].

This leaves the radial diffusion term, which takes the form

$$R(f_e) = \frac{1}{r}\frac{\partial}{\partial r} r \left[D_r(r,v)\frac{\partial}{\partial r} - V_r \right] f_e, \tag{4.3}$$

where the diffusion coefficient $D_r(r,v) = D_0 g(r) h(v)$ is a function of the radius and electron velocity. A convective velocity term V_r is used to balance the diffusion term to maintain the initial density profile. The radial component of the diffusion coefficient takes the form

$$g(r) = \left(C_1 + C_2 \left(\frac{r}{a} \right)^{C_3} \right)^{C_4} \left(\frac{n_e}{n_{e0}} \right)^{C_5} \left(\frac{T_e}{T_{e0}} \right)^{C_6} \left(\frac{Z_{eff}}{Z_{eff0}} \right)^{C_7}, \tag{4.4}$$

with default values of $C_1 = 1$, $C_2 = 3$, $C_3 = 3$, $C_4 = 1$, and $C_5 = C_6 = C_7 = 0$. The velocity component can be written as

$$h(v) = \frac{\left| \dfrac{v_\parallel}{v_{th(r=0)}} \right|^{C_1} \left(\dfrac{v_\perp}{v_{th(r=0)}} \right)^{C_3}}{\left(1 + \dfrac{L}{\lambda} \right)^{C_2} \gamma^{C_4}}, \tag{4.5}$$

where $L \equiv \pi q R$ is the autocorrelation length (q is the safety factor and R the major radius), λ is the mean free path, and γ is the relativistic factor. For a radial diffusion coefficient that increases with electron velocity, as in the case of stochastic magnetic field induced transport, $C_1 = 1$. For this case, setting $C_2 = 1$ provides a collisional reduction of the diffusion rate, as discussed by Rechester and Rosenbluth [14]. For a radial diffusion coefficient that is uniform in velocity space, as in the case of electrostatically induced transport, $C_1 = C_2 = 0$. In both cases, $C_3 = C_4 = 0$.

Numerical solutions are found from a Gaussian elimination of the implicitly-differenced Fokker-Planck equations on a defined set of flux surfaces. The equations are coupled using an alternating-direction-implicit (ADI) time advancement scheme. Particle flux is allowed at the spatial and velocity boundaries, and the distribution function is renormalized after every time step to match the measured density. The Fokker-Planck coefficients are calculated at the beginning of each time step. The code is run in a "partially-nonlinear" mode, where only the higher order Legendre polynomial terms in the Rosenbluth potentials are evolved, versus a linear mode (initial potentials are used throughout) or a nonlinear mode (fully evolved potentials are used) available in the code. This is the mode used for runaway electron studies, as it conserves particles and momentum while keeping the bulk distribution at the measured temperature and density. Choosing the proper time steps can show the evolution of the distribution function from a Maxwellian, while long time steps can be used for an iterative approach.

A module included in the CQL3D package calculates bremsstrahlung emission from electron-ion and electron-electron collisions, using the electron distribution func-

tion f_e calculated by the code [15]. The scattering background is assumed to be stationary. Each detector's line of sight is defined in the code, and the calculated flux is output as a line-integrated value that would be measured by each detector, expressed in units of energy per detector area, detector solid angle, time, and the energy range of interest ($\text{ergs} \cdot \text{cm}^{-2} \cdot \text{sr}^{-1} \cdot \text{s}^{-1} \cdot \text{eV}^{-1}$). These values are thus independent of detector geometry and can be compared directly to the measured fluxes, described in Chapter 3.

4.3.2 Using CQL3D to Model an RFP

The CQL3D code is used primarily to model tokamaks, but it has been successfully adapted for the topology of an RFP [16]. The initial Maxwellian distributions are known from Thomson scattering, ChERS, Rutherford scattering, and FIR interferometer measurements, all described in Chapter 2. MSTfit, used in conjunction with MSE spectroscopy and other MST diagnostics, provides the magnetic topology and current density profiles used by the code. This leaves only three unknowns when calculating the Fokker-Planck coefficients: the radial diffusion coefficient D_r, the effective ionic charge

$$Z_{eff} = \sum_Z Z^2 \frac{n_Z}{n_e}, \tag{4.6}$$

and the parallel electric field $E_\parallel$. Pollutant radiation from sources such as line emission and neutral bremsstrahlung have thwarted previous attempts to measure Z_{eff} from spectroscopy at longer wavelengths. X-ray spectroscopy, in conjunction with CQL3D, provides a new means by which Z_{eff} can be found.

Fig 4.5 shows how this is accomplished. The user inputs initial guesses for

the D_r and Z_{eff} profiles, and CQL3D computes an initial guess for $E_{\|}$ from the provided current profile and Spitzer resistivity. CQL3D then solves the Fokker-Planck equation for the electron distribution function f_e over a designated number of time steps and flux surfaces. The equation is solved through an iterative process for each time step and flux surface: the parallel current density $J_{\|}$ is computed from f_e after each iteration, and is compared to the value of $J_{\|}$ provided by MSTfit. The value of $E_{\|}$ is then adjusted for the next iteration, and the process continues until the two currents match. The code then moves on to the next flux surface, and when all flux surfaces have been completed, the next time step. Once the time steps are complete, the x-ray module calculates the expected flux from the final f_e. The user can then change the input D_r and Z_{eff} profiles and rerun the code. D_r and Z_{eff} are found from the run in which the calculated flux best fits the measured spectra.

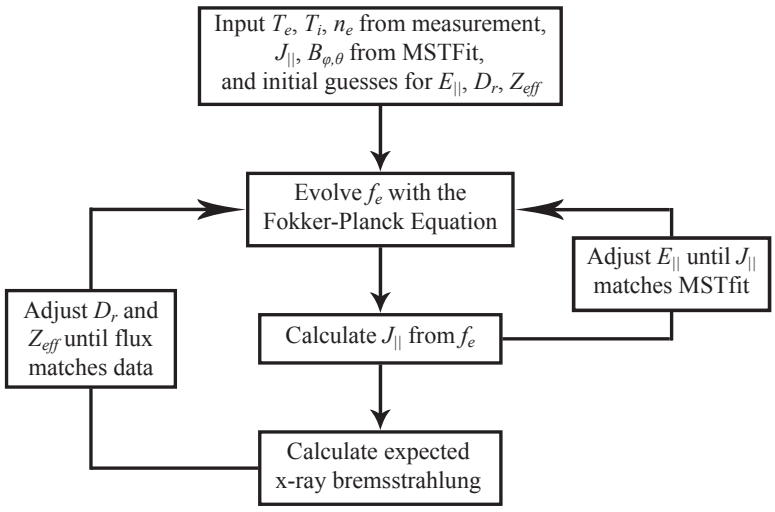

Figure 4.5: A chart demonstrating how CQL3D is used to find D_r and Z_{eff}.

The sxr detectors were added to the diagnostic to help decouple D_r from Z_{eff}. During most PPCD discharges, the hxr detectors only measure emission from extremely non-thermal electrons. The spectrum is relatively featureless, and its dependence on D_r can be difficult to distinguish from its dependence on Z_{eff}. With the sxr detectors, thermal electrons contribute to the lower energy flux, providing more information for the fit.

While CQL3D can accurately model the expected x-ray flux from a PPCD plasma, with its tokamak-like closed flux surfaces, attempts to model standard RFP discharges have thus far been unsuccessful. Choosing a radial diffusion rate proportional to electron velocity gives the best result, but still overestimates the measured x-ray flux. Most likely, transport in a standard RFP discharge is more complex than a simple Rochester-Rosenbluth model. If in the future transport in a standard RFP discharge is better understood, CQL3D may be able to model these plasmas using a more complex diffusion term.

4.3.3 Results

The key result from PPCD discharges is that setting $C_1 = 0$ in the velocity component of the diffusion coefficient (Eq. 4.5) gives the best fit to the measured x-ray spectra. In other words, the diffusion coefficient D_r becomes independent of electron parallel velocity. This is not consistent with stochastic transport but rather it is indicative of the formation of closed flux surfaces.

An example of a CQL3D fit to an sxr spectrum is shown in Fig 4.6. The spectrum is from a 400 kA PPCD discharge with a core electron temperature of about 900 eV and a core electron density of 0.9×10^{13} m^{-3}. The values that give the best fit to

the data are $D_r = 5.0$ m^2/s and $Z_{eff} = 5$. Since an increase in Z_{eff} or a decrease in D_r will both increase the hxr flux, it can be somewhat difficult to distinguish these two effects, though the change in the shape of the spectrum will differ slightly. Fig. 4.7 shows CQL3D x-ray spectra for $D_r = 100$ m^2/s, a poor guess for the diffusion coefficient. In this case none of the spectra match the data, regardless of the guess for Z_{eff}. A plot of the chi square of each fit is given in Fig. 4.8. It is clear from this figure that regardless of the value of D_r, Z_{eff} lies somewhere in the range of 4–6 for this discharge. When diffusion is turned off in the code, $Z_{eff} = 4$ gives the best fit to the data, and no run with $Z_{eff} > 6$ provides a proper fit, even with a sufficiently large D_r.

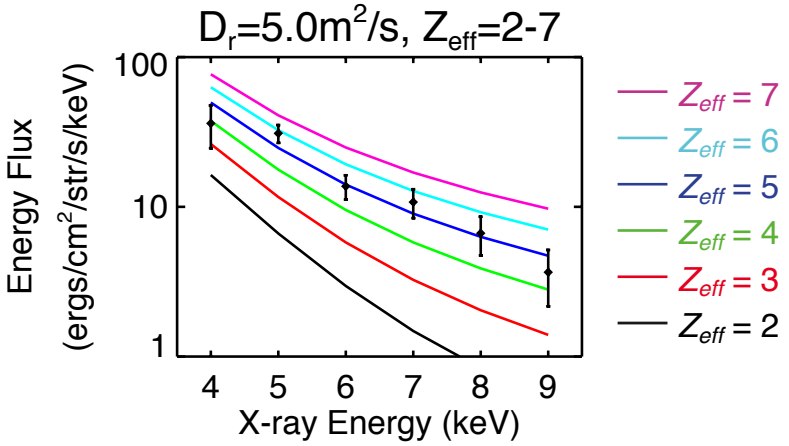

Figure 4.6: The solid lines represent CQL3D predictions for the spectrum for $D_r = 5.0$ m^2/s and for a range of Z_{eff} values. $Z_{eff} = 5$ gives the best fit to the data, represented by the points.

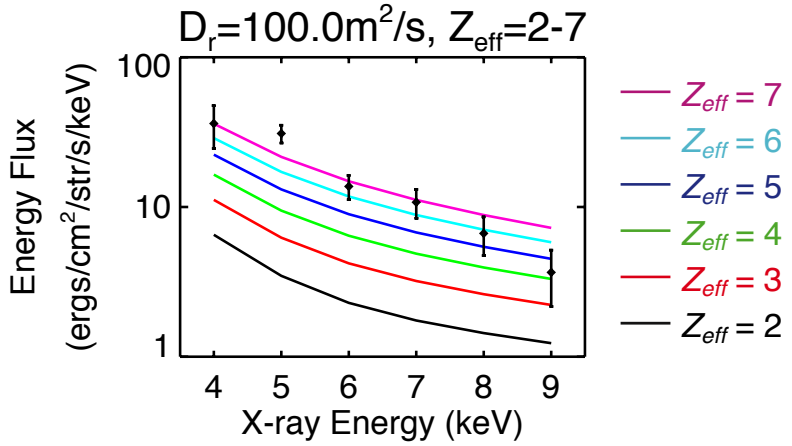

Figure 4.7: The same data as in Fig. 4.6, but with fits using $D_r = 100$ m^2/s. None of the fits match the data, regardless of the value of Z_{eff}.

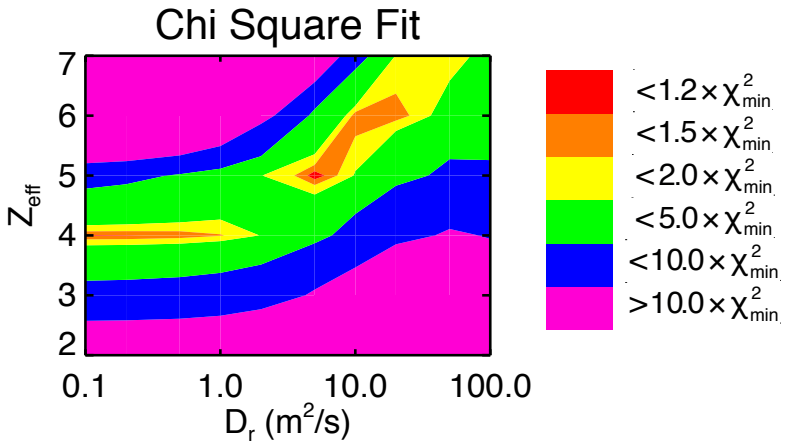

Figure 4.8: The chi square of the model's fit to the data for an array of D_r and Z_{eff} values, normalized to the value of the best fit.

4.4 Conclusions

X-ray spectroscopy has directly shown that not only does current profile modification reduce tearing mode amplitudes, but that it greatly reduces fast electron transport, and that this transport no longer depends on particle velocity. Therefore, stochasticity must be reduced, indicating that closed flux surfaces are restored in the core of the plasma. CQL3D has successfully been employed to demonstrate this point, and to quantify both the diffusion coefficient D_r and the effective ion charge Z_{eff}.

References

[1] C. R. Sovinec and S. C. Prager, Nucl. Fusion **39**, 777 (1999).

[2] J. S. Sarff, S. A. Hokin, H. Ji, S. C. Prager, and C. R. Sovinec, Phys. Rev. Lett. **72**, 3670 (1994).

[3] R. Bartiromo, V. Antoni, T. Bolzonella, A. Buffa, L. Marrelli, P. Martin, E. Martines, S. Martini, and R. Pasqualotto, Phys. Plasmas **6**, 1830 (1999).

[4] B. E. Chapman, T. M. Biewer, P. K. Chattopadhyay, C.-S. Chiang, D. J. Craig, N. A. Crocker, D. J. D. Hartog, G. Fiksel, P. W. Fontana, S. C. Prager, and J. S. Sarff, Phys. Plasmas **7**, 3491 (2000).

[5] J. K. Anderson, T. M. Biewer, C. B. Forest, R. O'Connell, S. C. Prager, and J. S. Sarff, Phys. Plasmas **11**, L9 (2004).

[6] M. R. Stoneking, N. E. Lanier, S. C. Prager, J. S. Sarff, and D. Sinitsyn, Phys. Plasmas **4**, 1632 (1997).

[7] J. S. Sarff, N. E. Lanier, S. C. Prager, and M. R. Stoneking, Phys. Rev. Lett. **78**, 62 (1997).

[8] B. E. Chapman, J. K. Anderson, T. M. Biewer, D. L. Brower, S. Castillo, P. K. Chattopadhyay, C.-S. Chiang, D. Craig, D. J. D. Hartog, G. Fiksel, P. W.

Fontana, C. B. Forest, S. Gerhardt, A. K. Hansen, D. Holly, Y. Jiang, N. E. Lanier, S. C. Prager, J. C. Reardon, and J. S. Sarff, Phys. Rev. Lett. **87**, 205001 (2001).

[9] B. E. Chapman, J. W. Ahn, A. F. Almagri, J. K. Anderson, F. Bonomo, D. L. Brower, D. R. Burke, K. Caspary, D. J. Clayton, S. K. Combs, W. A. Cox, D. Craig, B. H. Deng, D. J. D. Hartog, W. X. Ding, F. Ebrahimi, D. A. Ennis, G. Fiksel, C. B. Forest, C. R. Foust, P. Franz, S. Gangadhara, J. A. Goetz, M. C. Kaufman, J. G. Kulpin, A. Kuritsyn, R. M. Magee, M. C. Miller, V. V. Mirnov, P. D. Nonn, R. O'Connell, S. P. Oliva, S. C. Prager, J. A. Reusch, J. S. Sarff, H. D. Stephens, M. D. Wyman, and T. Yates, Nucl. Fusion **49**, 104020 (2009).

[10] R. W. Harvey and M. G. McCoy, in *Proc. of IAEA TCM on Advances in Simulation and Modeling of Thermonuclear Plasmas, Montreal, 1992*, pages 489–526, IAEA, Vienna (1993).

[11] D. J. Griffiths, *Introduction to Electrodynamics*, Prentice Hall, third edition (1999).

[12] G. D. Kerbel and M. G. McCoy, Phys. Fluids **28**, 3629 (1985).

[13] R. O'Connell, D. J. D. Hartog, C. B. Forest, J. K. Anderson, T. M. Biewer, B. E. Chapman, D. Craig, G. Fiksel, S. C. Prager, J. S. Sarff, and S. D. Terry, Phys. Rev. Lett. **91**, 045002 (2003).

[14] A. B. Rechester and M. N. Rosenbluth, Phys. Rev. Lett. **40**, 38 (1978).

[15] R. W. Harvey, X-ray energy spectra calculated from cql3d fokker-planck electron

distributions, Technical Report CompX-2000-2, CompX, P.O. Box 2672, Del Mar, CA 92014-5672 (2001).

[16] R. W. Harvey, O. Sauter, R. Prater, P. Nikkola, R. O'Connell, and C. B. Forest, in *Proc. 12th Joint Workshop in Electron Cyclotron Emission and Electron Cyclotron Resonance Heating (EC-12)*, pages 41–46 (2003).

Chapter 5

Improved Confinement within Magnetic Islands

5.1 Introduction

Another emerging route to globally improved confinement in the RFP is the single helicity state. The $m = 1$ tearing modes in standard plasmas are typically of about the same amplitude, but magnetohydrodynamic simulations have predicted that these modes can evolve spontaneously toward a single helicity state, where one mode, usually that resonant closest to the magnetic axis, grows to very large amplitude, while the other, secondary, $m = 1$ mode amplitudes vanish [1, 2]. The island associated with the dominant mode thereby produces a nonstochastic helical equilibrium in the RFP core. While pure single helicity has yet to be observed experimentally, the so-called quasi-single-helicity (QSH) mode spectra have been observed in several RFP plasmas [3–9]. In QSH spectra, the secondary modes do not vanish but often become smaller. In the RFX, RFX-mod, and MST RFP devices, soft-x-ray tomography reveals increased x-ray emission inside the island structure during QSH, suggesting a local

increase in the electron temperature [3, 4, 6, 8, 9]. This has been confirmed with Thomson scattering in RFX and RFX-mod [3, 4, 9], but there is not yet a robust temperature increase observed in MST. Most recently in RFX-mod, the dominant mode during QSH reached an amplitude large enough that the island enveloped the plasmas magnetic axis. This resulted in a substantially broader region of increased temperature and produced a several-fold improvement in global energy confinement [10]. Both the measured temperature increase and modeling of the magnetic topology during QSH imply reduced stochasticity and energy transport within the dominant magnetic island. However, there is as yet little experimental information concerning particle transport within the island.

This chapter describes data from MST from which it is deduced that within a single island in the plasma core, both stochasticity and particle transport are indeed reduced. The evidence for this is the emergence of high-energy runaway electrons in plasmas with an island in the core but without global confinement improvement. This is the first such observation in the RFP. That global confinement is not improved implies a localized region of reduced stochasticity. Reconstruction of the magnetic field topology and examination of the trajectory of high-energy test particles demonstrates both reduced stochasticity and reduced particle transport within the island. These observations include a variety of $m = 1$ mode spectra, ranging from QSH to cases where the innermost-resonant tearing mode is only weakly dominant. This is the first measurement of locally improved particle confinement in QSH plasmas.

5.1.1 Improved Confinement in Tokamak Islands

Particle transport within an island has previously been studied in the tokamak. Experiments performed on the TEXTOR tokamak have shown that magnetic islands can confine runaway electrons within an otherwise stochastic plasma [11]. In TEXTOR discharges with an electron density less than 10^{19} m^{-3}, runaways with energies up to 30 MeV emerged. Following injection of a deuterium pellet, large magnetic fluctuations developed, and field lines became stochastic. Runaway electrons were rapidly lost to the wall, with the exception of those residing within a remnant $m = 2, n = 1$ island. Within this island, runaway electrons remained well confined, forming a narrow helical beam of high-energy electrons within the otherwise stochastic plasma. The helical beam lasted for more than 0.6 s. While this experimental result supports the notion that an island embedded in an otherwise stochastic field can exhibit good confinement properties, it differs from the plasma conditions presented in this paper in that the tokamak plasma began in a nonstochastic state. In the RFP plasmas described here, the island emerges spontaneously within a stochastic field.

5.1.2 Plasma Conditions that Favor QSH

The measurements described herein were made in discharge conditions that in MST favor the appearance of QSH mode spectra. These conditions were discovered experimentally; the theoretical reasons these conditions favor QSH is not understood. To begin, QSH occurs most frequently in plasmas with high toroidal current and low density. Unless stated otherwise, the data presented throughout this chapter were taken from 400 kA discharges with line-averaged electron densities of about 5×10^{18} m^{-3}. Another important condition favoring QSH is zero toroidal magnetic field at

the plasma boundary, i.e., nonreversed plasmas. The safety factor or q profile for such a plasma is shown in Fig. 5.1. The equilibrium is distinguished by $q = 0$ at the boundary. Also note that the innermost resonant $m = 1$ mode has $n = 5$. This is usually the dominant mode.

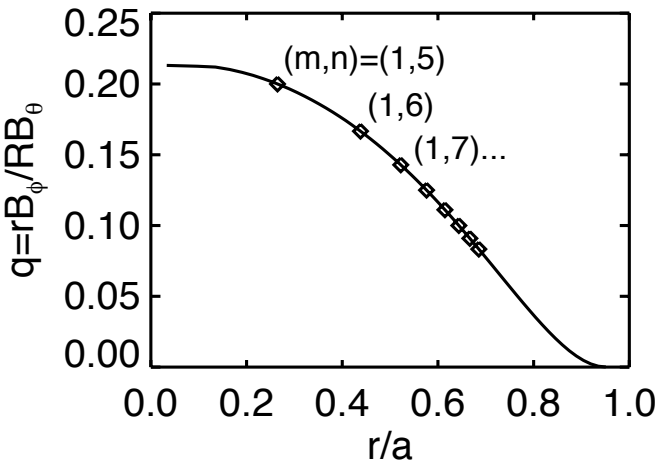

Figure 5.1: Safety factor profile from nonreversed discharges.

5.2 Correlation between HXR Flux and the Appearance of Islands

From a typical nonreversed discharge, Fig. 5.2 displays the temporal evolution of the central line-integrated hxr flux, two of the $m = 1$ mode amplitudes, the so-called spectral spread, and the toroidal plasma current. The spectral spread

$$N_S = \left[\sum_n \left(\frac{b^2_{\theta,(1,n)}}{\sum_n b^2_{\theta,(1,n)}} \right)^2 \right]^{-1}, \tag{5.1}$$

where the summation is from $n = 5$–14 in this analysis. N_S essentially reflects the number of $m = 1$ modes of significant amplitude or the degree of spectral peaking [12]. Pure single helicity mode spectra have $N_S = 1$. For MST plasmas, QSH mode spectra have historically (and somewhat arbitrarily) been identified by $N_S < 2$.

5.2.1 Correlation with Magnetic Modes

The hxr flux in Fig. 5.2 is somewhat correlated with the behavior of the $m = 1$ modes. Early in time, as the toroidal current is ramping up, the dominant $n = 5$ mode exhibits several periods during which it grows and then drops. The hxr flux shows roughly the same behavior. Later in time, after the toroidal current rise phase, there are two periods during which the $n = 5$ exhibits large amplitude for sustained periods. The width of the corresponding island, which is proportional to the square root of the mode amplitude, is also large. At the same time, the $n = 6$ mode as well as modes with $n > 6$ remain relatively small. Because of the very large $n = 5$ amplitude, N_S approaches 1 during these periods.

Leading up to 30 ms, the hxr flux grows, with a peak photon energy reaching > 100 keV. This energy is comparable to that observed in PPCD discharges, when stochasticity is reduced over much of the plasma. At 30 ms, the $n = 5$ mode amplitude drops suddenly, with a corresponding increase in the amplitudes of the $n \geq 6$ modes. This results in elimination of the hxr flux. Following 30 ms, the $n = 5$ mode grows again, with a corresponding re-emergence of the hxr flux. However, shortly after the n=5 mode amplitude reaches its peak, the hxr flux vanishes once again.

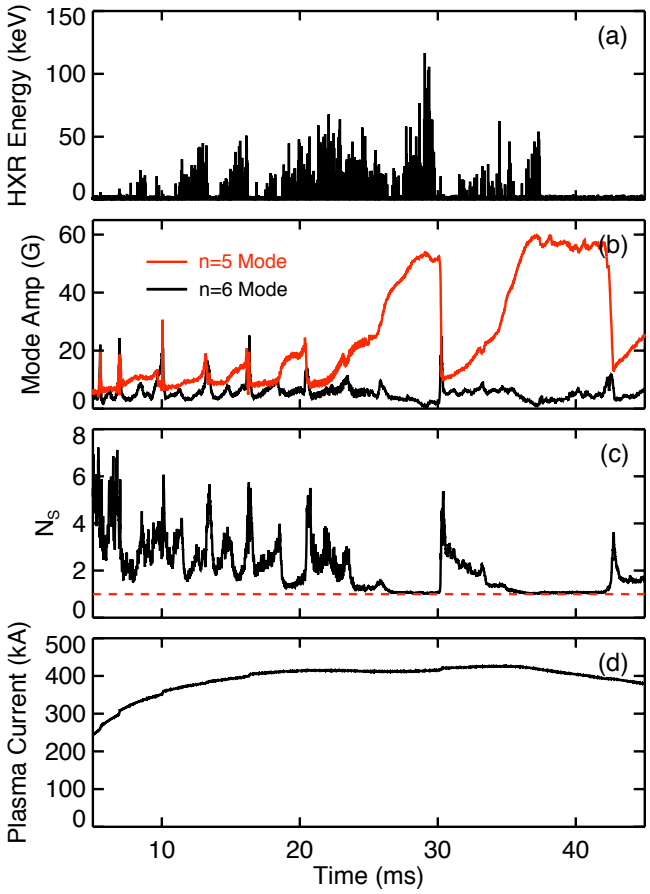

Figure 5.2: In a nonreversed discharge, temporal evolution of (a) the hard-x-ray counts from a central chord, (b) amplitudes of two $m = 1$ modes, (c) the spectral spread, defined in the text, and (d) the toroidal plasma current. Each hard-x-ray spike represents a measured photon. The red dashed line in (c) shows for reference the lower bound on the spectral spread. Shot 1061013015.

It is clear from Fig. 5.2 that N_S and hxr flux are only loosely correlated. However, on average the hxr flux is largest when N_S is small. This is illustrated in Fig. 5.3, which is based on an average of similar discharges. The hxr flux is largest for values of N_S usually associated with QSH, but there is finite flux for N_S up to 7, corresponding to a fairly broad $m = 1$ spectrum. The data in Figs. 5.2 and 5.3 reveal that the magnetic mode spectrum is not always useful as a predictor of the presence of hxr flux.

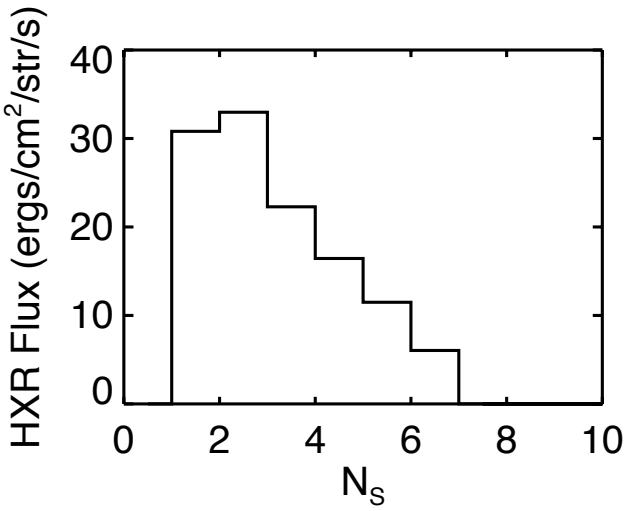

Figure 5.3: Dependence of hard-x-ray energy flux on spectral spread. Hard x rays with energies ranging from 10 to 150 keV are included. Histogram results from an average over several discharges similar to that in Fig. 5.2.

5.2.2 Correlation with SXR Tomography

A much better predictor is the presence of an island in the plasma core as indicated by sxr tomography. To illustrate this, Fig. 5.4 zooms in on some of the data shown in Fig. 5.2. Added to the top of the figure is sxr emissivity measured across a portion of the poloidal plasma cross section. The oscillating pattern in the sxr data corresponds to an $n = 5$ island rotating about the magnetic axis of the plasma, located at about 1.56 m. There is a clear correlation between the presence of the sxr island structure and the hxr flux. After 16.2 ms, the sxr island is disrupted for a short time as the $n = 5$ amplitude drops and the $n = 6$ amplitude rises, but the island is later restored along with the hxr flux. These data reveal not only a correlation between sxr structure and hxr emission, but they also reveal that a sxr structure (an island) can exist for $N_S > 2$.

Fig. 5.5 zooms in once again on data from the discharge in Fig. 5.2, and again includes sxr emissivity. This view is later in time at the period during which the $n = 5$ mode reaches a large amplitude and saturates, and hxr emission vanishes. Note that after 38 ms, the toroidal current begins to ramp down, and the electric field is no longer strong enough to generate new runaway electrons. This figure once again demonstrates the correlation between the sxr structure and hxr emission. Hard-x-ray emission vanishes when the hot island disappears, although a cooler island remnant may remain. It also demonstrates again that N_S is not a good predictor of either the sxr structure or hxr emission. Even with N_S very close to 1, its minimum possible value, there need not be a sxr structure in the plasma core. This figure also suggests a possible explanation, based on the behavior of the $n = 6$ and other secondary modes,

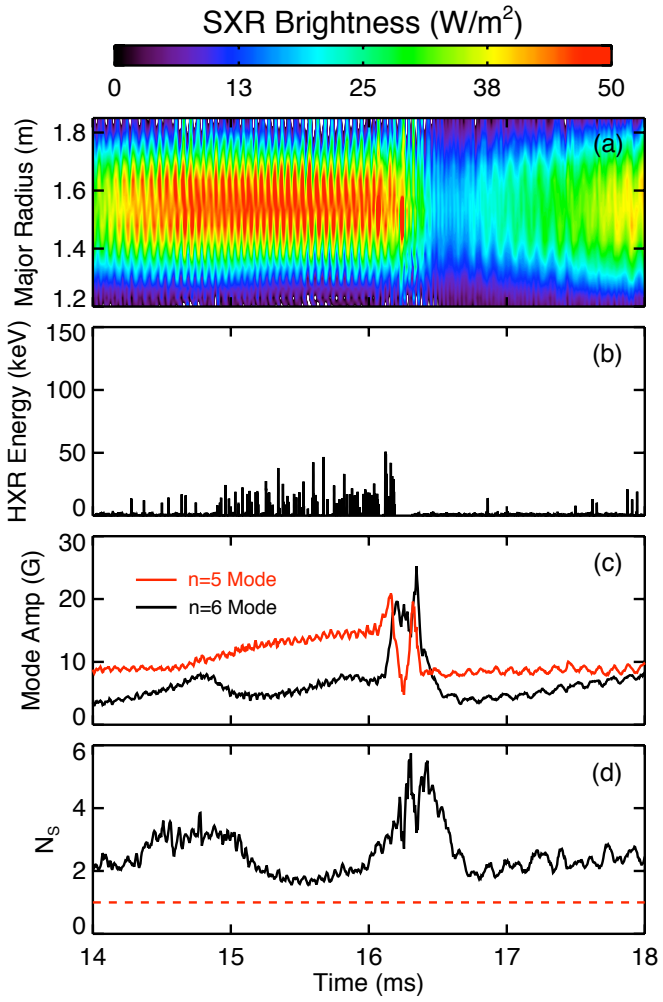

Figure 5.4: Zooming in on data from the discharge in Fig. 5.2: (a) sxr emission over the plasma cross section, (b) hxr counts, (c) amplitudes of two $m = 1$ modes, and (d) the spectral spread.

for the disappearance of the sxr structure and hxr emission. This topic is revisited at the end of the chapter.

5.3 Localization of Runaway Confinement

Thus far it has been demonstrated that the emergence of high-energy runaway electrons, requiring reduced stochasticity in the plasma, is well correlated with the presence of an island in the core. This is consistent with, but does not prove, the thesis that the runaway electrons are largely generated within the island. However, examination of the global energy confinement time and computational modeling further support the thesis.

5.3.1 Global Energy Confinement

Table 5.1 contains measurements of the global energy confinement time in MST in nonreversed and normal, reversed plasmas at two different densities. The energy confinement time is the ratio of the volume-integrated stored thermal energy to the volume-integrated Ohmic input power. The nonreversed, low-density case is the only one of the four discharges that exhibits an island. It is also the only case with a measurable hxr emission. All four cases have roughly the same 1 ms confinement time that is the norm for plasmas with a fully stochastic magnetic topology in the core. The energy confinement time increases tenfold during PPCD, when stochasticity is reduced throughout the core. The fact that the global confinement time in the plasmas examined here is only 1 ms requires that the region of reduced stochasticity and runaway electron generation be localized to a relatively small volume, as is the case with an island in the core.

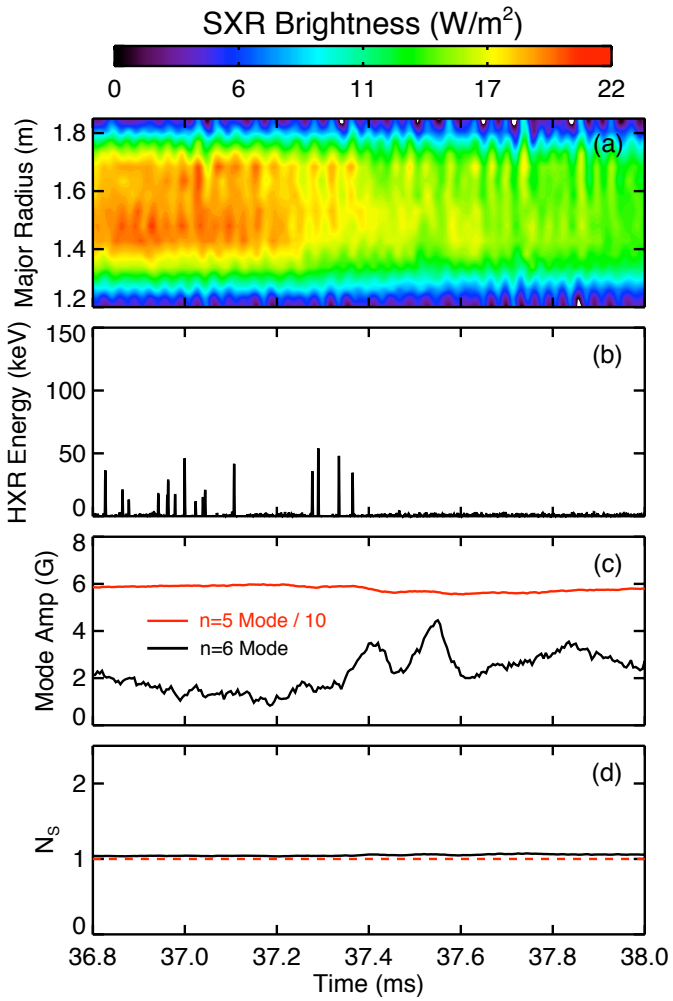

Figure 5.5: Zooming in again on data from the discharge in Fig. 5.2: (a) sxr emission over the plasma cross section, with a different brightness color mapping relative to Fig. 5.4, (b) hxr counts, (c) amplitudes of two $m = 1$ modes, with the dominant mode scaled down by a factor of 10, and (d) the spectral spread.

	$n_e = 0.5 \times 10^{19}$ m^{-3}	$n_e = 1.0 \times 10^{19}$ m^{-3}
Nonreversed	1.1 ms	1.5 ms
Reversed	0.7 ms	1.0 ms

Table 5.1: Global energy confinement times for nonreversed and reversed MST plasmas at two different line-averaged electron densities and a toroidal plasma current of 400 kA. Hard-x-ray emission is observed only in the non-reversed, low-density discharge.

5.3.2 Radial Profile of HXR Flux

Given that the core island is apparent in 2D sxr emission, it is natural to look for a similar signature in hxr data, with the premise that hxr emission might also be stronger within the island than without. Unfortunately, the hxr data are inconclusive, but they are instructive. In Fig. 5.6 is the hxr flux from a single detector in the radial array. This detector was chosen such that the rotating island regularly passes in and out of the detectors line of sight. The flux in Fig. 5.6 is plotted versus the location of the island's O-point in the poloidal plane. If hxr emission is enhanced within the island, one could reasonably expect the flux to depend on the islands position, but according to Fig. 5.6, it does not. The other detectors along the array provide the same result. This lack of island phase dependence may be due to substantial additional emission outside the island, both within the plasma and at the plasma-facing wall.

The case for hxr emission from the bulk plasma outside the island and from the plasma-facing wall is established by first examining the radial profile of hxr flux. In Fig. 5.7 is the radial profile of hxr flux for a typical nonreversed plasma with a magnetic island as well as a PPCD plasma. Each datum is a line-integrated flux, and the points

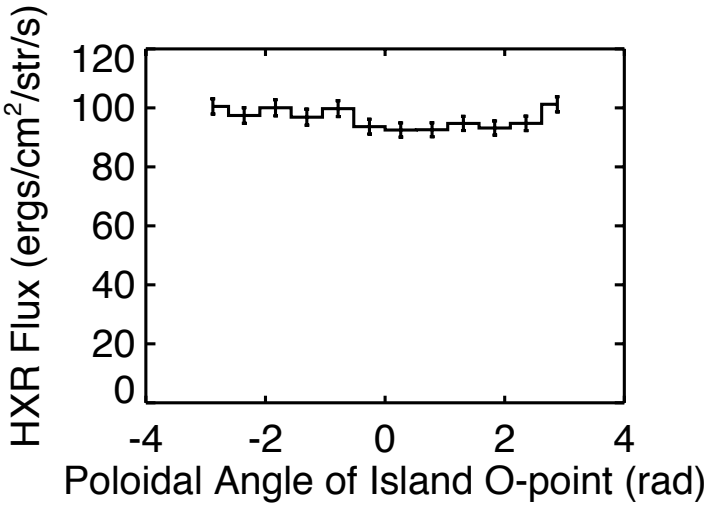

Figure 5.6: HXR flux from 10 to 150 keV versus the poloidal angle of the island O-point at the toroidal angle of the detector.

near $r/a = 0$ have the longest path lengths. The island in the nonreversed plasma resides well inside $|r/a| = 0.6$. The profile maxima are shifted outward, consistent with the usual outward shift of the magnetic axis, and both profiles exhibit the expected asymmetry due to the anisotropic angular distribution of relativistic bremsstrahlung. The profile from the PPCD plasma is peaked in the core region, where flux surfaces are restored and temperatures are the highest. By comparison, the nonreversed case shows a broader profile, implying a larger contribution from the plasma outside of $|r/a| = 0.6$ and/or from target emission at the plasma-facing wall. Also of note is that the two profiles are of similar magnitude. Although the runaway electrons in the nonreversed case are necessarily generated in a smaller volume than in the PPCD case, the loop voltage or accelerating electric field is roughly three times larger in the

nonreversed case [13], thereby generating a larger number of high-energy electrons more rapidly.

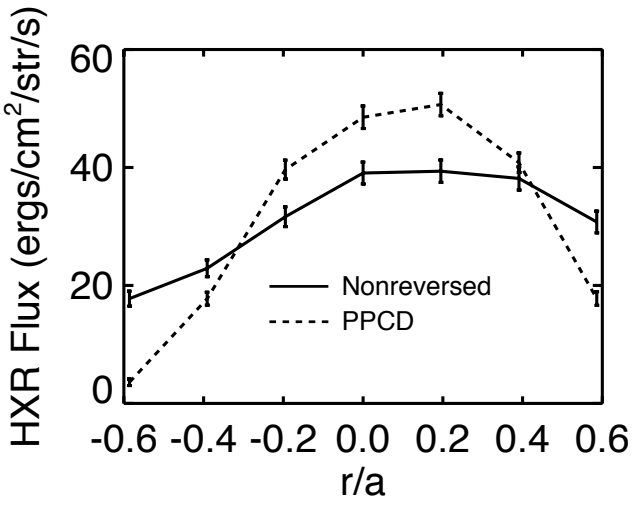

Figure 5.7: Including photon energies ranging from 10 to 150 keV, line-integrated hxr flux profiles from a nonreversed plasma discharge with a magnetic island and a discharge with PPCD.

5.3.3 Edge Measurements with a Target Probe

In several toroidal devices, hard-x-ray flux has been measured from runaways striking plasma limiters [14–16]. Evidence for similar emission at the plasma-facing wall in MST is provided by monitoring an insertable target probe, similar to the probes used in the ASDEK tokamak to measure the runaway population at a point near the plasma boundary [17]. On MST, a molybdenum-tipped probe was mounted on a port directly across from one of the hxr detectors and inserted 5 cm into the plasma. The

signal from this detector is compared to that obtained by the same detector when the probe was retracted. Data were gathered in nonreversed plasmas and in PPCD plasmas. Note that the flux measured by the other detectors was used as a control in these measurements. In each of the two sets of plasma, the flux measured by the other detectors exhibited little shot-to-shot variation and remained unchanged when the probe was inserted.

In Fig. 5.8(a) are hxr flux energy spectra during PPCD. When the target probe is inserted 5 cm into the plasma, the measured emission jumps by more than an order of magnitude. Runaway electrons that strike the solid target emit large amounts of bremsstrahlung, thus the large increase in emission demonstrates that there is a population of runaway electrons reaching the edge of the plasma. This is in sharp contrast to nonreversed plasmas, Fig. 5.8(b). Here, insertion of the probe makes very little difference in the measured flux. These data imply that only a tiny fraction of runaways reach the plasma-facing wall in the nonreversed case. Ruling out significant emission from the wall, the relatively flatter hxr flux profile in Fig. 5.7 is likely due in large part to spatially diffuse emission throughout the plasma volume.

Assuming that the only region of reduced stochasticity in these plasmas is within the island in the plasma core, one can easily speculate why there are high-energy electrons in the bulk plasma. It requires only finite transport of high-energy electrons across the island separatrix. Once outside the island, these electrons will then wander stochastically throughout the plasma volume, emitting bremsstrahlung along the way. The hxr data are thus incapable of providing the exact location where the electrons are accelerated to high energy. It is thus left to computational modeling to find this

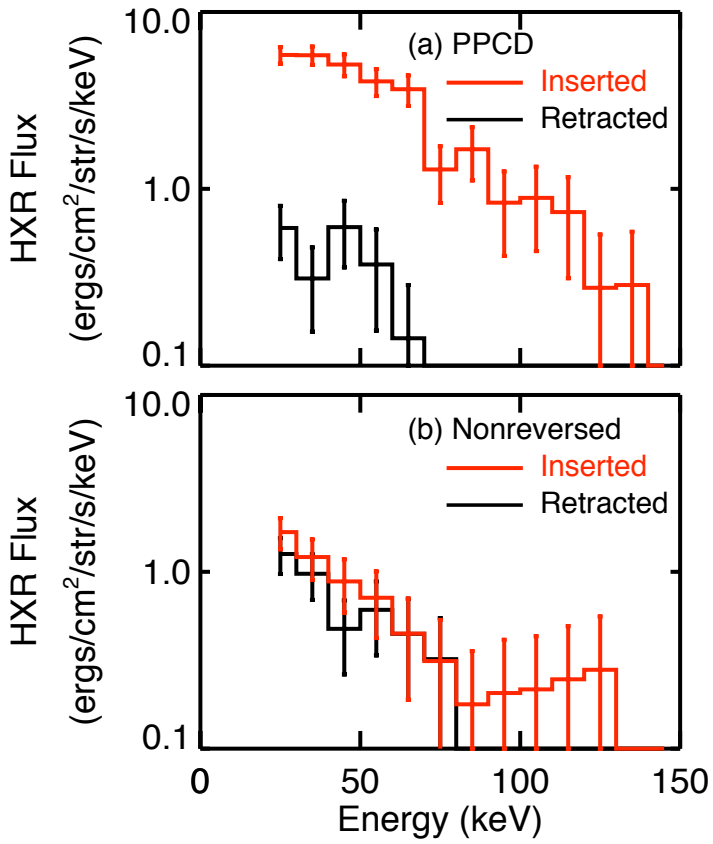

Figure 5.8: HXR energy spectra from a detector viewing an inserted target probe and the same detector viewing the fully retracted probe in (a) PPCD plasmas and (b) nonreversed plasmas.

region.

5.3.4 Computational Modeling with ORBIT

With computational modeling of both the magnetic topology and the trajectory of test particles placed in that topology, it is found that initially thermal electrons are accelerated to high energy within the island associated with the dominant $n = 5$ mode. The computation was performed with ORBIT, a Hamiltonian guiding center code [18]. ORBIT has been used in the recent past to predict the rate of transport of purely thermal electrons and ions in the presence of both fully stochastic and QSH (local reduction in stochasticity) magnetic topologies. The particle loss rate was found to be locally reduced within the island region in the QSH case [19, 20]. To simulate the plasmas described in this paper, the magnetic equilibrium is first reconstructed based on toroidal and poloidal field measurements at the MST plasma boundary and a standard RFP equilibrium model. The perturbation to the magnetic topology is calculated in ORBIT based on measurements of the tearing mode amplitudes using MSTs toroidal array of magnetic sensing coils. When the $n = 5$ mode is dominant in the $m = 1$ spectrum, ORBIT predicts the formation of an $n = 5$ island embedded in an otherwise stochastic background.

To initialize the test particle simulation, 1000 particles were placed within the island region. These particles had an effective initial temperature of 250 eV with random trajectories. A toroidal electric field of 1.5 V/m was applied. The particle trajectories were then allowed to evolve over about 2 ms. During this evolution, both pitch-angle and slowing-down collisions were included. The results of the simulation are shown in Figs. 5.9 and 5.10, which provide complementary views of the data.

Fig. 5.9 shows the distribution of electron energies, each electron represented by a dot, over the plasma minor radius, represented by poloidal flux. The vertical shaded band represents the width of the $n = 5$ island. The highest-energy electrons are located within the island, but there are also electrons well outside the island, consistent with what is expected from the experimental picture laid out in the last section. Although there are uncertainties in the experimental data used in the simulation, the largest electron kinetic energies seen in bulk are consistent with the hxr photon energies shown earlier, bearing in mind that only a fraction of the kinetic energy is emitted as radiation. The distribution of electron energies is plotted again in Fig. 5.10, this time versus poloidal and toroidal angle. Particles with an energy > 40 keV are indicated with red dots. Thus, the highest energy particles have an $m = 1, n = 5$ spatial distribution, consistent with their confinement within the $n = 5$ island.

In addition to modeling plasmas with a dominant $n = 5$ mode, cases were also examined in which all the mode amplitudes were comparable. Such a spectrum occurs just after 16.2 ms in Fig. 5.4. In such cases, ORBIT predicts a fully stochastic magnetic topology in the plasma core. Test particles deposited in the core undergo acceleration, but their maximum final energy is much lower than with an island present.

5.4 Conclusions

Hard x rays are emitted from MST plasmas with a magnetic island in the core. These high-energy photons arise from runaway electrons, requiring reduced stochasticity in the plasma. The global energy confinement time in these plasmas is comparable to that in plasmas with no hard-x-ray emission and with a fully stochastic magnetic field in the core. Hence, the region of reduced stochasticity is deduced to be localized

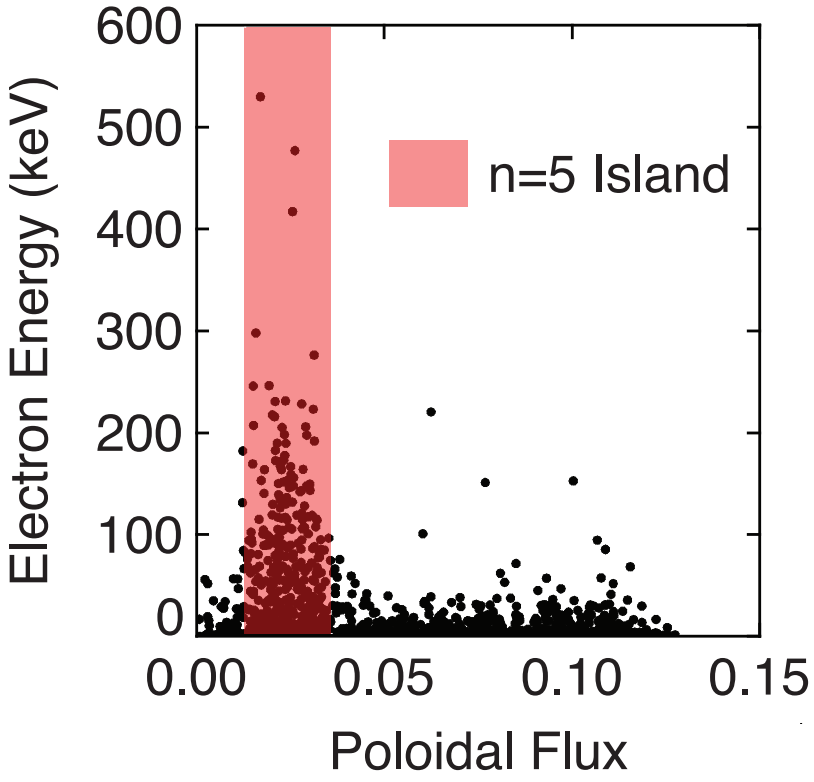

Figure 5.9: From a simulation with the ORBIT code, the final radial distribution of test electron energies after acceleration by an electric field. Each dot represents a single electron. The poloidal flux is a proxy for the radial coordinate. The shaded region indicates the width of the $n = 5$ island.

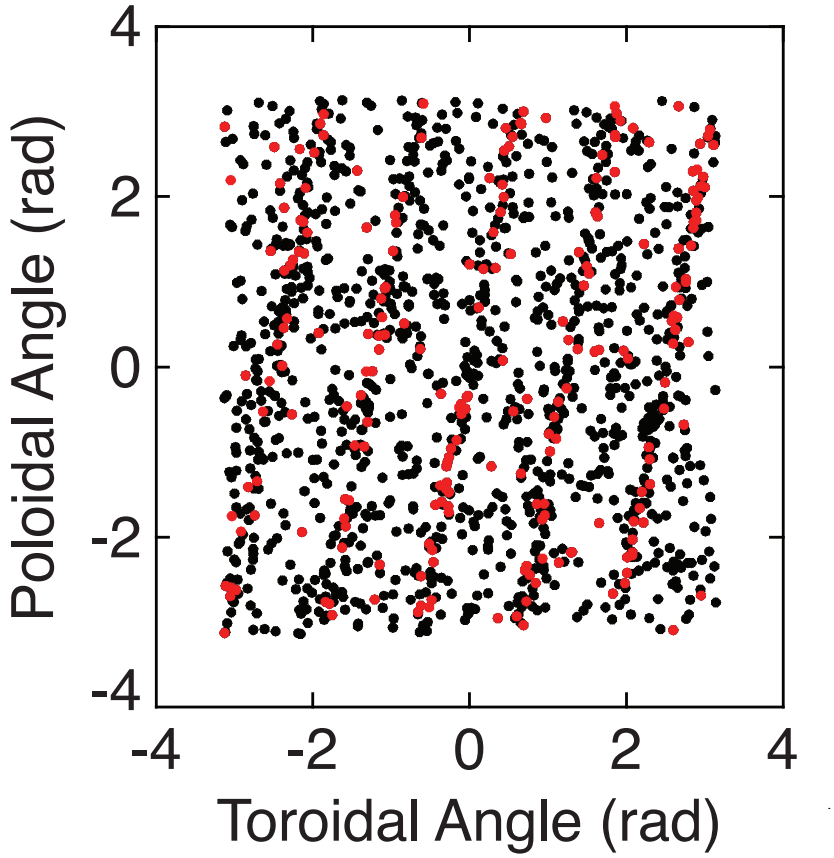

Figure 5.10: Final poloidal and toroidal positions of test electrons from the same simulation as in Fig. 5.9. Particles with an energy > 40 keV indicated with red dots.

to a relatively small volume. In a computational reconstruction of the magnetic field topology, an island emerges in the plasma core associated with the dominant mode. Test electrons placed within this island and undergoing acceleration by a toroidal electric field reach an energy comparable to that observed experimentally, and while the electrons diffuse across the plasma, the highest-energy electrons remain within the island. These results are similar to the previously discussed results from the TEXTOR tokamak, where high-energy runaway electrons can be well confined inside a magnetic island even when the surrounding plasma becomes stochastic. These experimental and computational data lead to the conclusion that stochasticity is indeed reduced within the island and that particle confinement is improved substantially therein.

It has also been shown that the degree of peaking of the $m = 1$ mode spectrum is insufficient to determine the presence or absence of an island, or at least a sxr structure, in the core. Even with a very large dominant mode, soft-x-ray tomography reveals that an associated sxr island structure is not always present. The determination of the presence of an island requires internal diagnosis of the plasma. This leads back to one lingering point from the discussion of Fig. 5.5. Although the dominant mode is very large in the time window displayed there, the island structure dissipates at one point, and hxr emission ceases. A possible explanation for this is found in the behavior of the secondary modes, represented in that figure by the $n = 6$ mode. This secondary mode amplitude increases at the same time the island structure begins to dissipate. Given the large amplitude of the dominant $n = 5$ mode, its associated island can overlap the $n = 6$ resonant surface. If the $n = 6$ mode amplitude becomes sufficiently large, this overlap will bring about stochasticity in that region. The fundamental point is that,

as has been noted elsewhere, the formation of a nonstochastic island by a single large mode depends not only on that mode being sufficiently large, but on the secondary modes being sufficiently small.

References

[1] S. Cappello and R. Paccagnella, Phys. Fluids B **4**, 611 (1992).

[2] J. M. Finn, R. Nebel, and C. Bathke, Phys. Fluids B **4**, 1262 (1992).

[3] D. F. Escande, P. Martin, S. Ortolani, A. Buffa, P. Franz, L. Marrelli, E. Martines, G. Spizzo, S. Cappello, A. Murari, R. Pasqualotto, and P. Zanca, Phys. Rev. Lett. **85**, 1662 (2000).

[4] P. Martin, A. Buffa, S. Cappello, F. D'Angelo, D. F. Escande, P. Franz, L. Marrelli, E. Martines, S. Ortolani, G. Spizzo, R. Bilato, T. Bolzonella, S. Costa, A. Murari, R. Paccagnella, R. Pasqualotto, D. Terranova, and P. Zanca, Phys. Plasmas **7**, 1984 (2000).

[5] L. Marrelli, P. Martin, G. Spizzo, P. Franz, B. E. Chapman, D. Craig, J. S. Sarff, T. M. Biewer, S. C. Prager, and J. C. Reardon, Phys. Plasmas **9**, 2868 (2002).

[6] P. Martin, L. Marrelli, G. Spizzo, P. Franz, P. Piovesan, I. Predebon, T. Bolzonella, S. Cappello, A. Cravotta, D. F. Escande, L. Frassinetti, S. Ortolani, R. Paccagnella, D. Terranova, the RFX team, B. E. Chapman, D. Craig, S. C. Prager, J. S. Sarff, the MST team, P. Brunsell, J.-A. Malmberg, J. Drake, the EXTRAP T2R team, Y. Yagi, H. Koguchi, Y. Hirano, the TPE-RX team, R. B.

White, C. Sovinec, C. Xiao, R. A. Nebel, and D. D. Schnack, Nucl. Fusion **43**, 1855 (2003).

[7] P. Piovesan, G. Spizzo, Y. Yagi, H. Koguchi, T. Shimada, Y. Hirano, and P. Martin, Phys. Plasmas **11**, 151 (2004).

[8] P. Franz, L. Marrelli, P. Piovesan, I. Predebon, F. Bonomo, L. Frassinetti, P. Martin, G. Spizzo, B. E. Chapman, D. Craig, and J. S. Sarff, Phys. Plasmas **13**, 012510 (2006).

[9] P. Martin, L. Marrelli, A. Alfier, F. Bonomo, D. F. Escande, P. Franz, L. Frassinetti, M. Gobbin, R. Pasqualotto, P. Piovesan, D. Terranova, and the RFX-mod team, Plasma Phys. Control. Fusion **49**, A177 (2007).

[10] R. Lorenzini, D. Terranova, A. Alfier, P. Innocente, E. Martines, R. Pasqualotto, and P. Zanca, Phys. Rev. Lett. **101**, 025005 (2008).

[11] R. Jaspers, N. J. L. Cardozo, K. H. Finken, B. C. Schokker, G. Mank, G. Fuchs, and F. C. Schüller, Phys. Rev. Lett. **72**, 4093 (1994).

[12] Y. L. Ho, D. D. Schnack, P. Nordlund, S. Mazur, H.-E. Satherblom, J. Scheffel, and J. R. Drake, Phys. Plasmas **2**, 3407 (1995).

[13] J. K. Anderson, T. M. Biewer, C. B. Forest, R. O'Connell, S. C. Prager, and J. S. Sarff, Phys. Plasmas **11**, L9 (2004).

[14] W. Bernstein, F. F. Chen, M. A. Heald, and A. Z. Kranz, Phys. Fluids **1**, 430 (1958).

[15] S. J. Zweben, D. W. Swain, and H. H. Fleischmann, Nucl. Fusion **18**, 1679 (1978).

[16] J. R. Myra, P. J. Catto, A. J. Wootton, R. D. Bengtson, and P. W. Wang, Phys. Fluids B **4**, 2092 (1992).

[17] O. J. Kwon, P. H. Diamond, F. Wagner, G. Fussmann, ASDEX, and N. Teams, Nucl. Fusion **28**, 1931 (1988).

[18] R. B. White and M. S. Chance, Phys. Fluids **27**, 2455 (1984).

[19] I. Predebon, L. Marrelli, R. B. White, and P. Martin, Phys. Rev. Lett. **93**, 145001 (2004).

[20] M. Gobbin, L. Marrelli, P. Martin, and R. B. White, Phys. Plasmas **14**, 072305 (2007).

Chapter 6

Summary and Conclusions

In summary, x-ray spectroscopy is used to measure fast electron transport in the MST reversed-field pinch. A small fraction of the electron population runs away in the applied electric field, and these fast electrons emit x-ray bremsstrahlung as they scatter off of background ions. A measurable hard-x-ray flux indicates an improvement in particle confinement: standard RFP plasmas have stochastic field lines, and fast electrons radially diffuse out of the core before they reach high enough energies to emit hard x rays.

The x-ray spectroscopy diagnostic consists of twelve CdZnTe hard-x-ray detectors and a Si soft-x-ray detector, with five new Si detectors just recently added to the system. The detectors are primarily placed along a radial array of seventeen vacuum port windows, though a few detectors are placed at other toroidal locations. Each detector package consists of a photodiode and preamplifier, and the signal is sent through a Gaussian shaping amplifier. The signal is digitized, and Gaussians are fit to the resulting pulses to resolve pileup and separate signal from noise. Apertures limit the etendue to prevent pulse pileup while filters prevent saturation by low energy x rays.

When pulsed parallel current drive is applied to an MST discharge, a large flux of hard x rays is detected. The core-peaked x-ray flux grows exponentially in time at the beginning of PPCD, then saturates. The flux quickly disappears at the end of PPCD. This is indicative of closed flux surface restoration and particle transport that is no longer dominated by magnetic fluctuations. The Fokker-Planck code CQL3D can be used to model the electron distribution function and quantify both the radial diffusion coefficient D_r and the effective ion charge Z_{eff}. For a typical 400 kA PPCD discharge, $D_r = 5$ m^2/s and $Z_{eff} = 5$.

Hard x rays are also detected when a magnetic island spontaneously forms in the core of the plasma, as seen with soft-x-ray tomography. This usually occurs when the $m = 1$ magnetic mode spectrum exhibits quasi-single helicity. However, the x-ray flux disappears when the secondary modes grow large, regardless of the magnitude of the dominant mode. It is thought that closed flux surfaces form within the island and confine fast electrons, though the evidence is not conclusive. The absence of any change in the global energy confinement time indicates that improved particle confinement is limited to some small region, and modeling with the ORBIT code indicate that this region is inside the island, but the measured x-ray flux is spatially diffuse. This is most likely because fast electrons escape the island and wander stochastically about the plasma volume.

The initial questions laid out in the introduction have now been answered:

- *Why did the x-ray flux not match the CQL3D model at high energies?*

  High-energy x rays were escaping the vacuum vessel and striking the detector crystals. The hard-x-ray detectors are now surrounded by lead boxes, which

block these x rays and provide better fits to CQL3D.

- *How might apertures and filters, which are required to measure larger fluxes without saturating the detector amplifiers, affect the measurements?*

  When the data is properly normalized, the result appears independent of the apertures and filters used, and matches expected spectra from CQL3D.

- *What does an array of detectors reveal about the radial profile of hxr flux during PPCD?*

  The flux profile peaks in the core as expected, indicating that flux surfaces are restored in this region. Relativistic beaming of the bremsstrahlung emission causes the profile to be asymmetric, making the measurement difficult to invert.

- *With the addition of a soft-x-ray detector to expand the measured spectrum, can CQL3D be used to find Z_{eff}, thus allowing for a more accurate measurement of D_r?*

  With the sxr spectrum, Z_{eff} can be inferred from CQL3D, at least in the case of PPCD.

- *Do other types of RFP plasmas emit hard x rays, an indication of reduced stochasticity and improved confinement? Do these plasmas behave in a fashion similar to PPCD plasmas?*

  Plasmas with a single, large, magnetic island also emit hard x rays, similar to plasmas with PPCD. However, in these plasmas, fast electrons are only generated in a localized region within the island, then wander stochastically about the plasma.

With the new array of sxr detectors and with improved modeling, new questions might be answered in the future:

- *How do D_r and Z_{eff} vary radially in PPCD plasmas?*
- *Can diffusion within magnetic islands be modeled with another Fokker-Planck code using helical flux surfaces?*
- *Can diffusion in standard RFP discharges be better understood using a more sophisticated diffusion model, such as one assuming a mixed magnetic topology with interspersed regions of stochastic fields and closed flux surfaces* [1]*?*
- *Can the effects of EBW or LH wave injection on the electron distribution function be seen via x-ray spectroscopy?*

In conclusion, magnetic flux surfaces can be restored and particle confinement can vastly improve with the reduction of the $m = 1$ tearing modes. One mode may be large, as is the case with QSH, but the other modes must remain small enough to prevent any overlap. If the RFP is ever to achieve success as a fusion device, the tearing modes must clearly be suppressed. PPCD has proven successful as a means of suppressing the modes, but only transiently. Experiments using radio frequency wave injection may one day succeed in modifying the current profile for a longer period of time. As RFPs increase in current and temperature, it appears that they will tend towards single helicity mode spectra. However, it is not yet clear if this will improve confinement to a point that is acceptable for a fusion reactor.

References

[1] C. C. Hegna and J. D. Callen, Phys. Fluids B **5**, 1804 (1993).

Appendix A

X-Ray Radiation Doses from MST: A Worst Case Scenario

A high current, high temperature PPCD discharge produces a larger flux of hard x rays than any other plasma discharge studied on MST. The hard-x-ray flux measured during high current PPCD is in good agreement with modeling results obtained with the Fokker-Planck code CQL3D, supporting the accuracy of the measurements. Along the radial array, the line of sight with the largest measured flux is typically the one that views the outward-shifted magnetic axis. The largest flux measured in the hxr range along this line of sight is about 10 ergs $\cdot$ cm^{-2} $\cdot$ sr^{-1} $\cdot$ s^{-1} $\cdot$ keV^{-1} at 10 keV, and drops exponentially at higher energies, as shown in Fig. A.1. This approximates the flux that would be measured at the inside wall of the machine; the 5 cm thick aluminum vacuum vessel should strongly attenuate any x-ray flux that escapes the machine. The flux expected to escape the machine is plotted in Fig. A.2. Photons with energies lower than 10 keV cannot penetrate even a thin sheet of aluminum and should not escape the vessel.

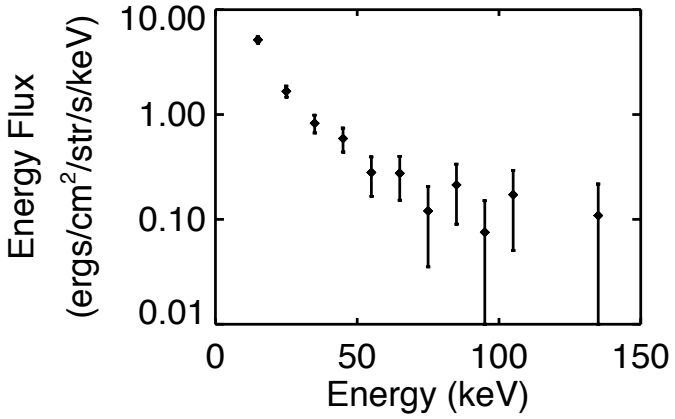

Figure A.1: X-ray spectra measured along a line of sight near $r/a = 0.1$ during a typical high-current PPCD plasma.

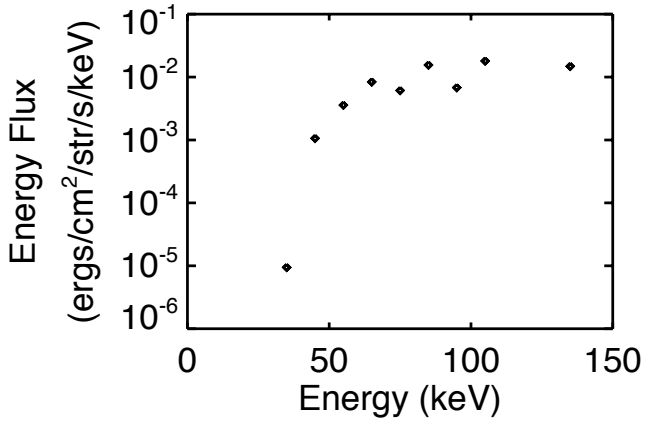

Figure A.2: Expected flux through the 5 cm aluminum shell. Note that x rays above 150 keV have not been detected on MST.

A.1 Worst Case: Laying on top of MST during a High Current PPCD Discharge

From Fig. A.2, the energy flux that penetrates the wall is less than 2×10^{-2} ergs$\cdot$ cm$^{-2} \cdot$ sr$^{-1} \cdot$ s$^{-1} \cdot$ keV^{-1} from about 50 keV to 150 keV. Integrating over time (the duration of PPCD is about 10 ms) and energy (a range of 100 keV), the maximum energy flux per unit of etendue is 2×10^{-2} ergs $\cdot$ cm$^{-2} \cdot$ sr^{-1}. Assuming MST occupies half of the surface area of a sphere encompassing a nearby person (2π steradians), and assuming this person has 175 cm x 50 cm of surface area facing the machine (a 5'9" person), and assuming all radiation that hits this person is absorbed, he or she would absorb about 1100 ergs of ionizing radiation per shot.

$$\frac{2 \times 10^{-2} \text{ ergs}}{\text{cm}^2 \cdot \text{sr} \cdot \text{s} \cdot \text{keV}} \times (175 \times 50 \text{ cm}) \times 2\pi \text{ sr} \times 0.01 \text{ s} \times 100 \text{ keV} = 1100 \text{ ergs} \qquad \text{(A.1)}$$

Converting to joules, a 70 kg person would absorb 1.6×10^{-6} J/kg, or 1.6×10^{-6} Gy of radiation. Since the quality factor of x-ray radiation is 1, this is the equivalent of a 1.6×10^{-6} Sv radiation dose. Assuming an exposure to 20 run days of 50 shots each (1000 total shots), a person would be exposed to 1.6 mSv in a year. For comparison, background radiation from natural sources is 2.4 mSv per year.

$$\frac{1100 \text{ ergs/shot}}{70 \text{ kg}} \times \frac{10^{-7} \text{ J}}{\text{ergs}} \times \frac{1000 \text{ mSv}}{1 \text{ J/kg}} \times \frac{1000 \text{ shots}}{\text{yr}} = \frac{1.6 \text{ mSv}}{\text{yr}} \qquad \text{(A.2)}$$

The US Nuclear Regulatory Commission's occupational limit is 50 mSv per year. Of course, no MST worker would be laying directly on top of the machine during a discharge. As a person moves away from the machine, the solid angle and thus the

total radiation dose would drop as the distance squared. Additionally, concrete walls should strongly attenuate any x-ray flux reaching someone in the control room. This is consistent with measurements by radiation badges placed around the machine, which have shown safe levels of radiation exposure.